Roh *et al. Energy Mater.* **2025**, *5*, 500061
DOI: 10.20517/energymater.2024.219

Energy Materials

Review

Open Access

Check for updates

Towards practical all-solid-state batteries: structural engineering innovations for sulfide-based solid electrolytes

Jihun Roh[1], Namgyu Do[1], Hyungjin Lee[1], Sangki Lee[2], Jangwook Pyun[2], Seung-Tae Hong[1,3,4,*], Munseok S. Chae[2,*]

[1]Department of Energy Science and Engineering, DGIST (Daegu Gyeongbuk Institute of Science and Technology), Daegu 42988, Republic of Korea.
[2]Department of Nanotechnology Engineering, Pukyong National University, Busan 48513, Republic of Korea.
[3]Department of Chemistry and Chemical Biology, University of New Mexico, Albuquerque, NM 87131, USA.
[4]NexeriaTek Inc., Daejeon 34016, Republic of Korea.

[*]**Correspondence to:** Prof. Munseok S. Chae, Department of Nanotechnology Engineering, Pukyong National University, 45 Yongso-ro Nam-gu, Busan 48513, Republic of Korea. E-mail: mschae@pknu.ac.kr

How to cite this article: Roh, J.; Do, N.; Lee, H.; Lee, S.; Pyun, J.; Hong, S. T.; Chae, M. S. Towards practical all-solid-state batteries: structural engineering innovations for sulfide-based solid electrolytes. *Energy Mater.* **2025**, *5*, 500061. https://dx.doi.org/10.20517/energymater.2024.219

Received: 20 Oct 2024 **First Decision:** 19 Nov 2024 **Revised:** 1 Dec 2024 **Accepted:** 9 Dec 2024 **Published:** 28 Feb 2025

Academic Editor: Xiongwei Wu **Copy Editor:** Ping Zhang **Production Editor:** Ping Zhang

Abstract

Sulfide-based solid electrolytes have emerged as pivotal components for the advancement of next-generation all-solid-state batteries, owing to the battery safety and higher energy density. This paper reviews the recent material innovations in sulfide-based solid electrolytes, focusing on enhancing their ionic conductivities based on an understanding of their crystal structures. Through a comprehensive analysis of current research trends and future perspectives, this review aims to provide a roadmap for the development of more robust and efficient sulfide-based solid electrolytes, which contribute to the realization of safer and higher-performance all-solid-state batteries.

Keywords: All-solid-state batteries, sulfide solid electrolyte, super ionic conductor, thio-germanate

INTRODUCTION

Transitioning to a more sustainable and energy-efficient future heavily relies on advancements in

lithium-ion battery (LIB) technology, particularly for electric vehicles (EVs) and energy storage systems (ESSs)[1]. As EVs and ESSs play a pivotal role in realizing Net Zero Emissions by 2050, many countries and cities have declared their plans to ban internal combustion engine vehicles within 10 to 30 years and replace them with EVs[2,3]. However, EVs and ESSs currently face two main challenges: energy density and safety. At present, EVs have a limited driving range of 150-300 miles per single charge, which is a critical threshold for their commercial success[2,3]. Considering the constraints of space and weight in EVs, batteries with higher energy densities are essential for enabling longer driving distances. Currently, LIBs at the cell level have energy densities of 260-295 Wh kg^{-1} and 650-730 Wh L^{-1}, which approaches their theoretical limits[4,5]. However, the targets for EVs set by the U.S. Department of Energy and the U.S. Advanced Battery Consortium for advanced batteries are 350 Wh kg^{-1} and 750 Wh L^{-1} at the cell level[6]. This indicates that the current LIB technologies still fall short of these goals.

The recent commercialization of portable devices, EVs, and ESSs using LIBs has highlighted significant safety concerns[7,8]. Notable incidents, such as the Samsung Galaxy Note 7 explosions, Boeing 787 Dreamliner battery fires, and frequent explosions in current EVs, underscore the urgent need to address these issues[9]. The primary cause of these incidents was the use of low-flash-point organic solvents in conventional organic liquid electrolyte LIBs such as ethylene carbonate and dimethyl carbonate[10]. These limitations necessitate comprehensive improvements across the entire battery system, particularly for the materials used for the cathode, anode, electrolyte, and separator.

Developing all-solid-state batteries (ASSBs) that replace conventional liquid-based electrolytes with solid electrolytes is a solution that can overcome these challenges. The solid nature of these electrolytes facilitates a broader operational temperature range and reduces the risk of ignition compared to flammable organic liquid electrolytes[11-15]. Additionally, solid electrolytes may enable the use of high-energy-density lithium metal anodes by preventing dendrite growth, which is a critical issue in liquid electrolytes and can lead to short circuits[16,17]. Moreover, the absence of electrolyte leakage in solid-state batteries enables the bipolar stacking of battery modules, shifting from the monopolar design commonly used in current LIBs with liquid electrolytes[18]. Furthermore, the dry-electrode processing design displays the potential for higher energy density through the adoption of high-loading composite electrodes (> 6 mAh cm^{-2})[19]. In liquid-based LIBs, limitations in transport and wettability restrict the maximum areal loading. Therefore, ASSBs can enhance both the volumetric and gravimetric energy densities of the battery system, and offer a higher energy density and improved safety compared with traditional liquid-based LIBs[19]. Figure 1A-C illustrates the operational temperature range of typical electrolyte types, two types of stacking of battery modules, and calculated volumetric and gravimetric energy densities of ASSBs based on cell parameters. ASSBs with thin sulfide solid electrolytes (SSEs, ~30 μm) that adopt high-loading composite electrodes enable a gravimetric energy density surpassing 350 Wh kg^{-1}, and meet the targets set by the U.S. Department of Energy and the U.S. Advanced Battery Consortium for advanced batteries in EVs.

Current liquid electrolytes in LIBs typically consist of $LiPF_6$ in mixtures such as ethylene carbonate with dimethyl carbonate or propylene carbonate, and exhibit an ionic conductivity of 1-10 mS cm^{-1} at room temperature[15]. To match or enhance the performance of the current LIBs, the ionic conductivity of solid electrolytes must be comparable to that of liquid electrolytes, which necessitates significant advancements in this field. Major breakthroughs include the discovery of room-temperature ionic conductors such as garnet-type structure[22], $Li_{10}GeP_2S_{12}$ (LGPS)[12], argyrodite family[23,24], and thio-Lithium Ion Superionic CONductors (thio-LISICONs)[25-27], which exhibit lithium ionic conductivities ranging from 0.1 mS cm^{-1} to 10 mS cm^{-1}, comparable to those of the liquid electrolytes.

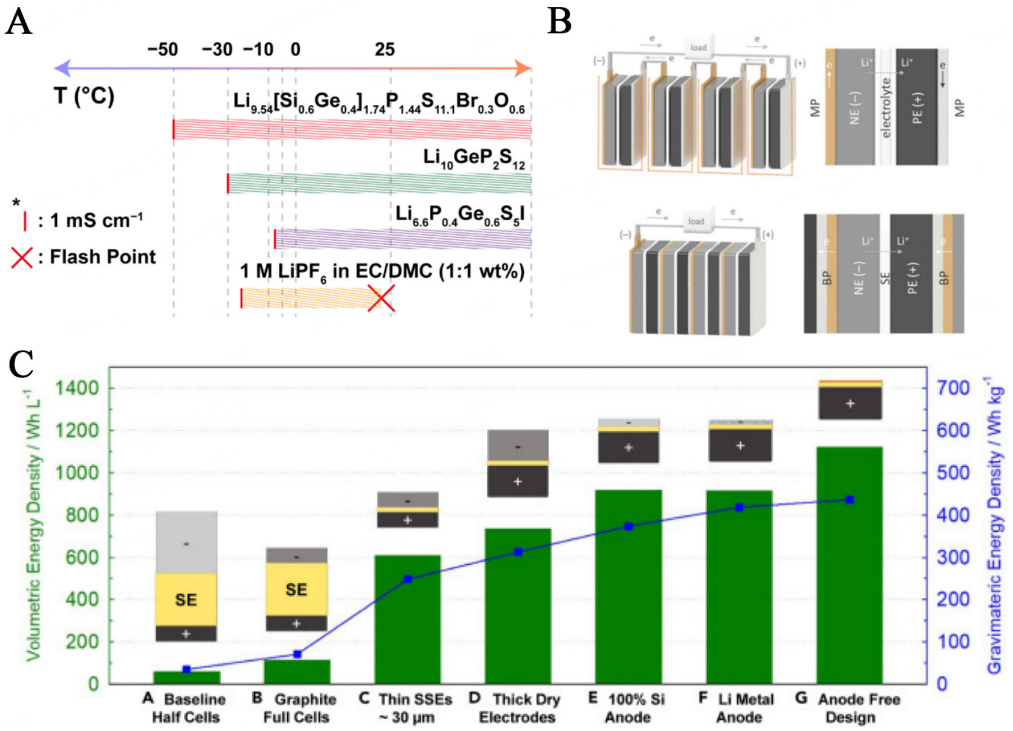

Figure 1. (A) Operational temperature range of typical electrolyte types, including both liquid and solid electrolytes. Each electrolyte type is represented by a different color. The dashed bars indicate the temperature ranges for specific electrolytes as follows: Red for $Li_{9.54}[Si_{0.6}Ge_{0.4}]_{1.74}P_{1.44}S_{11.1}Br_{0.3}O_{0.6}$ [20], green for $Li_{10}GeP_2S_{12}$ [12], violet for $Li_{6.6}P_{0.4}Ge_{0.6}S_5I$ [21], and orange for 1 M $LiPF_6$ in EC/DMC (1:1 wt%)[15]. The lower temperature limits for all the electrolytes are determined based on their ionic conductivity, specifically when it reaches approximately ~1 mS cm^{-1}. The flash point is indicated by a red cross[11]; (B) Schematic of a monopolar design of liquid-type battery (top) and a bipolar design of ASSBs (bottom)[18]. Reproduced with permission[18] Copyright 2019, Wiley-VCH GmbH; (C) Calculated volumetric and gravimetric energy densities of ASSBs based on cell parameters[19]. Reproduced with permission[19]. Copyright 2022, Elsevier. ASSBs: All-solid-state batteries; EC/DMC: ethylene carbonate/dimethyl carbonate.

Sulfides, known for their high polarizability, include many well-known superionic conductors with conductivities reaching up to 32 mS cm^{-1} at room temperature within the various discovered lithium ionic conductors[13,20,28]. Moreover, owing to their softness, the grain boundaries within the particles were significantly reduced by cold pressing the powders[29]. Consequently, the sintering process, which is typically required to reduce the grain boundaries in oxide-based solid electrolytes, can be omitted after cell assembly[30-32]. This simplification makes them more practical for the scalable fabrication of ASSBs.

Figure 2 shows the Arrhenius plots of various solid electrolyte structures, highlighting sulfides as having the highest ionic conductivity among all types. SSEs can be categorized into two main types: crystalline structures and glass. Typical crystalline structures of SSEs include the argyrodite family (Li_6PS_5X, where X = Cl, Br, or I)[23], LGPS[12], and thio-LISICONs (typical composition Li_xMS_4, where M = Al, Si, P, Ga, Ge, Sn, or Sb)[27,40-46]. Glass materials primarily consist of precursors such as Li_2S (which provides mobile ions) and M_xS_y (where M_x represents the stoichiometric amount of framework ions of B, Al, Si, P, Ge, Sn, or Sb and y indicates the stoichiometric amount of sulfur required to balance the valency of M_x)[47-51] with variations in the ratios of these precursors. The key difference between the crystal structures and glass is that the latter has less-ordered lithium ion diffusion pathways, which can result in relatively high conductivity owing to the more random arrangement of lithium ions or vacancies that form suitable pathways through the material[52]. However, this randomness can limit the extent to which the ionic conductivity can be further improved. In contrast, while it is challenging to identify a lithium-ion-conducting crystalline structure,

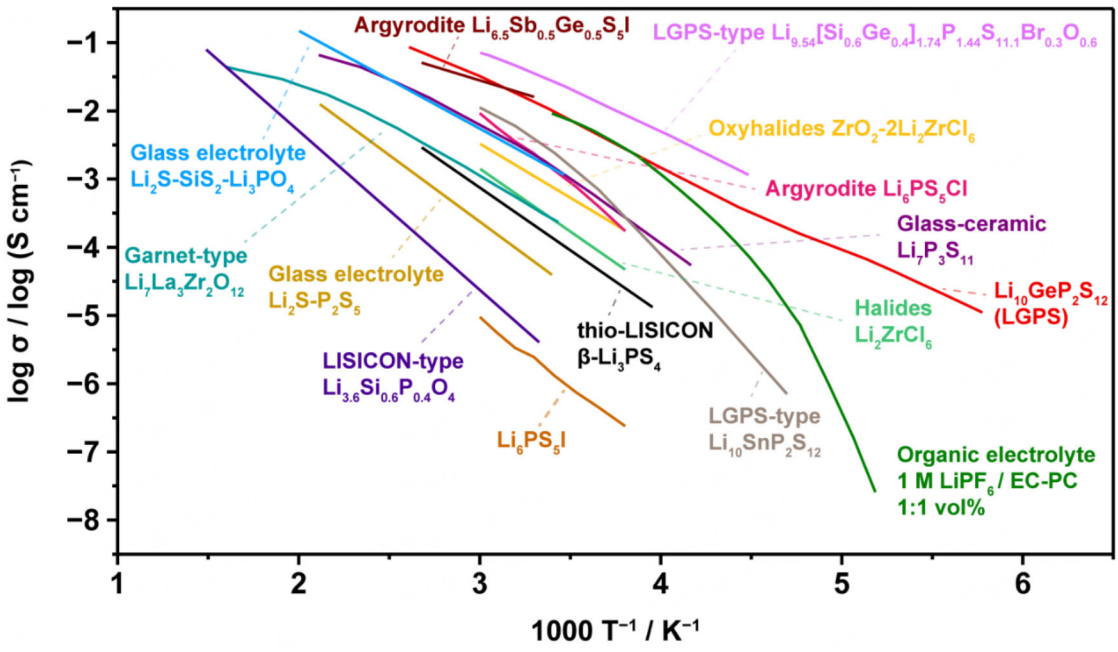

Figure 2. Arrhenius plots of various types of solid electrolytes, including organic liquid electrolytes, glass, and crystalline solid electrolytes[12,15,20,22,26,28,33-39].

those that present a suitable diffusion network have the potential to possess significantly high ionic conductivity, potentially surpassing that of glass. This hypothesis is supported by ongoing research and results, which is why there is considerable interest in the development and optimization of crystalline materials[12,13,53,54].

Because lithium-ion diffusion persists within the crystal structure framework, the type of anion stacking configuration may affect the conduction behavior. Wang *et al.* found that the *bcc* anion sublattice exhibits the lowest activation barrier for lithium-ion conduction, as lithium ions migrate between the face-sharing tetrahedral sites within a network that is energetically equivalent[55].This is in contrast to the common hexagonal close-packed (*hcp*) or face-centered cubic (*fcc*) anion frameworks, in which lithium ions must migrate through sites with dissimilar coordination numbers (4 and 6). This variation in coordination numbers results in different energy barriers for achieving percolation owing to the differing site energies associated with each coordination number. While the superionic conductors LGPS and $Li_7P_3S_{11}$ adopt a *bcc* anion sublattice, high ionic conductivity has also been observed in non-*bcc* anion sublattice structures, such as argyrodites Li_6PS_5X (X = Cl, Br, and I). This is attributed to the lithium-ion pathways that percolate through the face-sharing tetrahedral sites within the crystal structure, which is a conduction mechanism that mirrors the percolation observed in the *bcc* anion sublattice structures[55].

Conventionally, the ionic conductivity of crystals is mainly attributed to four factors: (1) the concentration of carrier ions or vacancies, (2) the dimensions of the mobile ion diffusion channels, (3) the polarization of the framework ions, and (4) minimal changes in the coordination environment along the diffusion pathways[36,56-59]. Specifically, ionic conductivity can be defined by[56]:

$$\sigma = nq\mu = NcZ_iq\mu_i \quad (1)$$

where n is the concentration of the carrier ions (number of ions cm^{-3}), Z_i is the integer number of charges of the ith charge carrier, q is the charge of an electron (C), and μ_i is the mobility of the i^{th} ion [cm^2 $(V\ s)^{-1}$]. The concentration n can be defined as the product of the density of ion sites in the sublattice of interest N (number of ions cm^{-3}) and the fractional occupation of the ions c. The ionic mobility μ_i is defined by the Einstein relation[56]:

$$\mu_i = \frac{Z_i q D_i}{k_B T} \tag{2}$$

Where D_i corresponds to diffusion coefficient (cm^2 s^{-1}), and k_B is the Boltzmann constant (J K^{-1}). Again, the diffusion coefficient can be described using conventional hopping theory[56]:

$$D = D_0 \exp\left(-\frac{\Delta G}{k_B T}\right) = \gamma(1 - c)Za^2 v_0 \exp\left(\frac{\Delta S}{k_B}\right) \exp\left(-\frac{E_m}{k_B T}\right) \tag{3}$$

Where γ is the geometrical factor that considers different crystal structures that the diffusion geometry is in, $(1 - c)Z$ is the number of neighboring unoccupied sites as Z is the number of nearest neighbors, a is the jump distance (cm), v_0 is the attempt frequency (s^{-1}) which corresponds to the oscillator frequency of moving cations, ΔS is the entropy of migration (J K^{-1}), and E_m is the migration energy (J). Consequently, the ionic conductivity can be expressed as[56]:

$$\sigma = \gamma \frac{N(Z_i q)^2}{k_B T} c(1 - c)Za^2 v_0 \exp\left(\frac{\Delta S}{k_B}\right) \exp\left(-\frac{E_m}{k_B T}\right) \tag{4}$$

$$\sigma = \frac{\sigma_0}{T} \exp\left(-\frac{E_a}{k_B T}\right) \tag{5}$$

where E_a is the activation energy for the conduction of mobile ions, which is similar to the migration energy E_m. In the expression for σ, the product of $c(1 - c)Z$ must be nonzero for the material to function as an ionic conductor, where $(1 - c)Z$ represents atomic defects, particularly vacancies and interstitial sites. The exponential part of the equation corresponds to the entropy term associated with ion migration and activation energy, both of which are key parameters that significantly influence ionic conductivity[56]. Therefore, reducing the activation energy is of considerable interest for enhancing ionic conductivity. From the perspective of lattice dynamics, the polarizability of the framework ions is correlated to the activation energy[58]. Higher polarizability increases the distance between the mobile and framework ions, which results in weaker bonds and, therefore, reduces the activation energy[36,60]. Furthermore, the ionic motion within a unit cell is highly affected by the type of crystal structure, which can be considered as a geometrical factor, γ, in the ionic conductivity equation[56]. Overall, achieving a high ionic conductivity requires an optimal concentration of ionic carriers and vacancies, low activation energy, high entropy, and a crystal structure specifically optimized for ionic conduction.

In this review, we systematically investigate various SSE systems, including glassy sulfides, thio-LISICONs (Li_xMS_3 and Li_xMS_4, where M = Al, Si, P, Ga, Ge, Sn, and Sb), the $Li_{10}MP_2S_{12}$ family (M = Si, Ge, Sn), and argyrodite compounds such as Li_6PS_5X (X = Cl, Br, and I). The ion-conduction mechanism is explained in relation to the crystal structure type, and further material designs aimed at enhancing ion conduction are illustrated.

SULFIDE SOLID ELECTROLYTES: STRUCTURAL ASPECT

Table 1 presents the ionic conductivity and activation energy of the SSEs. The structural characteristics of these electrolytes, including both glassy phases and various crystalline structures, were systematically

Table 1. Ionic conductivity and activation energy of sulfide solid electrolytes. Room temperature corresponds to the temperature region of 298-303 K

Material (mole fraction)	σ_{RT} (S cm^{-1})	E_a (eV)	Reference
60Li_2S-40P_2S_5	1.3 × 10^{-5}	0.5	[61]
67Li_2S-33P_2S_5	6.6 × 10^{-5}	0.42	[61]
70Li_2S-30P_2S_5	1.6 × 10^{-4}	0.40	[61]
75Li_2S-25P_2S_5	2.8 × 10^{-4}	0.39	[62]
80Li_2S-20P_2S_5	1.3 × 10^{-4}	0.4	[62]
55(66Li_2S-33P_2S_5)-45LiI	~ 10^{-3}	0.3	[63]
67(75Li_2S-25P_2S_5)-33$LiBH_4$	1.6 × 10^{-3}	0.22	[64]
40LiI-60Li_4SnS_4	4.1 × 10^{-4}	0.43	[65]
70Li_2S-30B_2S_3	9.5 × 10^{-5}	0.43	[61]
67Li_2S-23B_2S_3-10P_2S_5	1.4 × 10^{-4}	0.40	[61]
70(75Li_2S-10B_2S_3-15P_2S_5) -30LiI	1.5 × 10^{-3}	0.19	[66]
50Li_2S-50SiS_2	1.5 × 10^{-4}	0.34	[67]
72.7Li_2S-18.2P_2S_5-9.1SiS_2	5.0 × 10^{-4}	0.29	[50]
72.7Li_2S-18.2P_2S_5-9.1GeS_2	5.2 × 10^{-4}	0.27	[50]
72.7Li_2S-18.2P_2S_5-9.1SnS_2	3.5 × 10^{-4}	0.35	[50]
5Li_2S-3SiS_2	1.2 × 10^{-3}	0.30	[68]
γ -Li_3PS_4	3.0 × 10^{-7}	0.49	[27]
β-Li_3PS_4	2.0 × 10^{-4}	0.36	[69]
α-Li_3PS_4	1.3 × 10^{-3}	0.33	[69]
$Li_{10}GeP_2S_{12}$	1.2 × 10^{-2}	0.25	[12]
$Li_{9.54}Si_{1.74}P_{1.44}S_{11.7}Cl_{0.3}$	2.5 × 10^{-2}	0.24	[13]
$Li_{9.81}Sn_{0.81}P_{2.19}S_{12}$	5.5 × 10^{-3}	0.26	[70]
$Li_{10.35}Si_{1.35}P_{1.65}S_{12}$	6.7 × 10^{-3}	0.27	[70]
Li_2GeS_3	1.6 × 10^{-8}	0.37	[71]
Orthorhombic-Li_2SiS_3	2.0 × 10^{-6}	0.49	[72]
$Li_{1.82}SiP_{0.036}S_3$	2.4 × 10^{-3}	0.28	[25]
Li_2SnS_3	1.5 × 10^{-5}	0.59	[73]
Li_4GeS_4	2.0 × 10^{-7}	0.53	[74]
LT-Li_4SiS_4	9.4 × 10^{-7}	0.36	[41]
HT-LI_4SiS_4	5.3 × 10^{-7}	0.40	[41]
$Li_7P_3S_{11}$	3.2 × 10^{-3}	0.12	[75]
Li_6PS_5Cl	1.9 × 10^{-3}	0.22	[76]
Li_6PS_5Br	6.8 × 10^{-3}	0.27	[76]
Li_5PS_5I	4.6 × 10^{-7}	0.32	[76]
$Li_{5.5}PS_{4.5}Cl_{1.5}$	9.4 × 10^{-3}	0.29	[77]
$Li_{5.3}PS_{4.3}Br_{1.7}$	1.1 × 10^{-2}	0.18	[78]
$Li_{6.7}Si_{0.7}Sb_{0.3}S_5I$	1.1 × 10^{-2}	0.26	[24]
$Li_{6.6}P_{0.4}Ge_{0.6}S_5I$	1.2 × 10^{-2}	0.21	[79]

investigated. This analysis provides insight into the relationship between the crystal structure, ionic conductivity, and activation energy of these materials.

Glasses

Glasses were first recognized for their ion-conducting properties in 1884 when Warburg demonstrated the ability of sodium ions to pass through Thüringer glass under the influence of an electric field applied between two sodium amalgams[80]. The highest lithium-ion conductivities reported in oxide glasses are

typically 10^{-7}-10^{-4} S cm^{-1} at 473 K[81-83], while sulfide-based glasses exhibit higher ionic conductivities even at room temperature[50,61,84,85]. The increased polarizability and lower charge density of the sulfide anions reduce the Coulombic interactions between the mobile cations and sulfur anions, which causes weaker bonding. This, in turn, allows for higher ionic conductivity[30,36].

The most systematically studied glass sulfide is the binary xLi$_2$S-(100-x)P$_2$S$_5$ system (where x represents the mole percentage). The short-range order of the PS$_4$ framework exhibited different sharing modes depending on its composition [Figure 3A and B]. A higher concentration of alkali modifiers, such as Li$^+$, caused a reduction in network connectivity by creating nonbridging sulfur anions, similar to what was observed in the oxide systems[86]. As the proportion of x in the xLi$_2$S-(100-x)P$_2$S$_5$ binary system increased, the network connectivity of the PS$_4^{3-}$ units became more isolated. This progressive isolation eventually resulted in a dominant phase characterized by isolated PS$_4$ building blocks at x = 75, which evolved from the corner-shared forms of PS$_3^-$ or P$_2$S$_7^{4-}$. Consequently, the highest ionic conductivity was observed at x = 75, and was measured to be 2.8 × 10^{-4} S cm^{-1} at room temperature[62]. In this regard, it is assumed that the different types of polyanion building blocks (PS$_4^{3-}$, P$_2$S$_6^{4-}$, and P$_2$S$_7^{4-}$) which existed in an amorphous state within the xLi$_2$S-(100-x)P$_2$S$_5$ system, played an important role in determining Li-ion conductivity[62,84]. However, recent computational studies on this binary system have indicated a weak correlation between the polyanionic environment and the ionic conductivity. Lithium diffusivity was consistent across different polyanionic structures, which challenges the traditional view. Instead, the primary factor for ionic conductivity in the glass system is the connectivity of lithium-ion pathways rather than specific local environments such as polyanion arrangements[87].

Unlike the Li$_2$S-P$_2$S$_5$ binary glass system, recent studies on Li$_2$S-SiS$_2$ binary systems have highlighted the importance of the Si-S polyanion type [Figure 3C and D]. Specifically, two edge-sharing SiS$_4$ (Si$_2$S$_6^{4-}$) units exhibited weaker lithium attraction than the isolated SiS$_4^{4-}$ tetrahedral building block, as supported by both experimental data and the Ab-initio random structure searching technique [Figure 3E and F]. Among the compositions studied, 5Li$_2$S-3SiS$_2$, which contains the Si$_2$S$_6^{4-}$ unit, exhibited the highest ionic conductivity at room temperature (1.2 × 10^{-3} S cm^{-1}) compared with 2Li$_2$S-SiS$_2$ and 6Li$_2$S-4SiS$_2$, both of which contained only isolated SiS$_4^{4-}$ units[68]. Overall, these findings collectively underscore the importance of considering both the lithium-ion pathway network connectivity and polyanion building block features when optimizing glassy electrolytes to enhance lithium-ion conduction.

Crystalline materials

Li-P-S glass ceramics

Inorganic glassy compounds comprising sulfides crystallize when heated to specific temperatures. These crystalline structures are classified as glass-ceramics[88]. The most well-known glass-ceramics are Li$_2$P$_2$S$_6$ (50Li$_2$S-50P$_2$S$_5$), Li$_7$P$_3$S$_{11}$ (70Li$_2$S-30P$_2$S$_5$), Li$_3$PS$_4$ (75Li$_2$S-25P$_2$S$_5$), Li$_7$PS$_6$ (87.5Li$_2$S-12.5P$_2$S$_5$), and Li$_4$P$_2$S$_6$ (67Li$_2$S-33P$_2$S$_5$)[27,89-94]. Similar to glass materials, the framework of these structures is highly dependent on the specific ratio of their precursors. The regular and repeating frameworks of the crystalline structure and the ionic conductivities of the crystallites are more strongly influenced by the arrangement of the polyanion building blocks than by those of the glasses[55,95-98]. Because Li$_3$PS$_4$ and Li$_7$PS$_6$ have thio-LISICON and argyrodite crystal structures, respectively, they are discussed in a later section. This section focuses on the crystal structures of Li$_2$P$_2$S$_6$, Li$_4$P$_2$S$_6$, and Li$_7$P$_3$S$_{11}$.

Figure 4A and B shows the crystal structure of Li$_2$P$_2$S$_6$. The crystalline Li$_2$P$_2$S$_6$ structure was first identified by Eckert *et al.* using nuclear magnetic resonance (NMR) spectroscopy[101]. Later, Dietrich *et al.* further elucidated the solvation of the crystal structure[89], and both studies revealed edge-sharing PS$_4$ tetrahedral

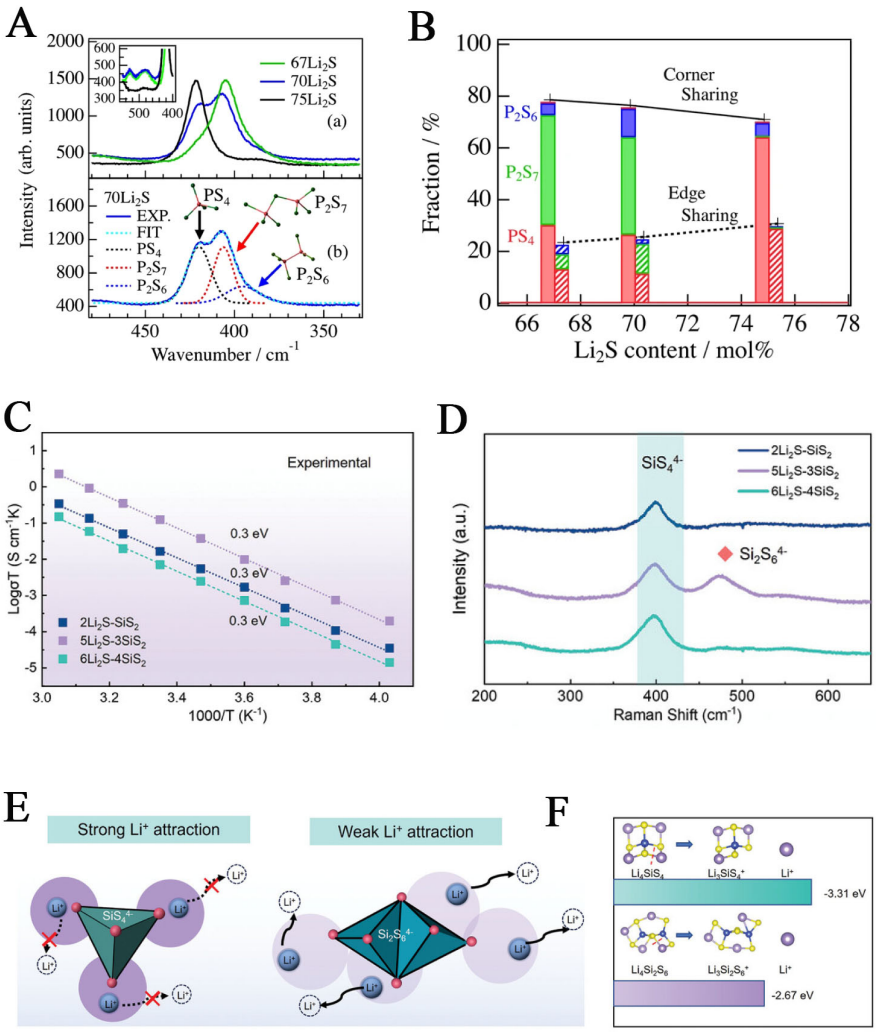

Figure 3. (A) Raman spectra for Li_2S-P_2S_5 glasses. $75Li_2S$, $70Li_2S$, and $67Li_2S$ glasses are represented in black, blue, and green lines, respectively[84]; (B) Calculated polyhedral connection statistics of Li_2S-P_2S_5 glasses using DFT/RMC model. The filled and hatched bars represent corner and edge-sharing[84]. Reproduced with permission[84]. Copyright 2016, Springer Nature; (C) Arrhenius plots and (D) Raman spectra for the $2Li_2S$-SiS_2, $5Li_2S$-$3SiS_2$, and $6Li_2S$-$4SiS_2$; (E) Schematics of Li^+ attraction and (F) dissociation energy of Li^+ in two different polyhedral unit, SiS_4^{4-} and $Si_2S_6^{4-}$ [68]. Reproduced with permission[68]. Copyright 2024, Wiley-VCH GmbH. DFT/RMC: Density functional theory/reverse Monte Carlo.

units ($P_2S_6^{2-}$) within a unit cell. $Li_2P_2S_6$ crystallized in the monoclinic space group $C2/m$ (no. 12), and two edge-sharing PS_4 ($P_2S_6^{2-}$) were formed in an eclipsed arrangement along specific axes. The lithium ions were located within the basal-distorted octahedral sites, and formed chains with an edge-shared form [Figure 4C]. The low ionic conductivity (7.8×10^{-11} S cm^{-1} at room temperature) and high activation energy (0.48 eV) observed for the $Li_2P_2S_6$ can be explained by three main factors: (1) the absence of three-dimensional (3D) isotropic diffusion that prevented long-range lithium-ion transport, (2) the high activation energy barrier between different jumps along the chains, and (3) the fully occupied lithium-ion sites within a unit cell, which resulted in a limited number of available sites for hopping. To summarize, the main cause of the lower ionic conductivity in the $Li_2P_2S_6$-type crystal structure is the deficiency of charge carriers. Therefore, chemical tuning with aliovalent ions to control the charge-carrier concentration can enhance the lithium-ion conductivity of $Li_2P_2S_6$.

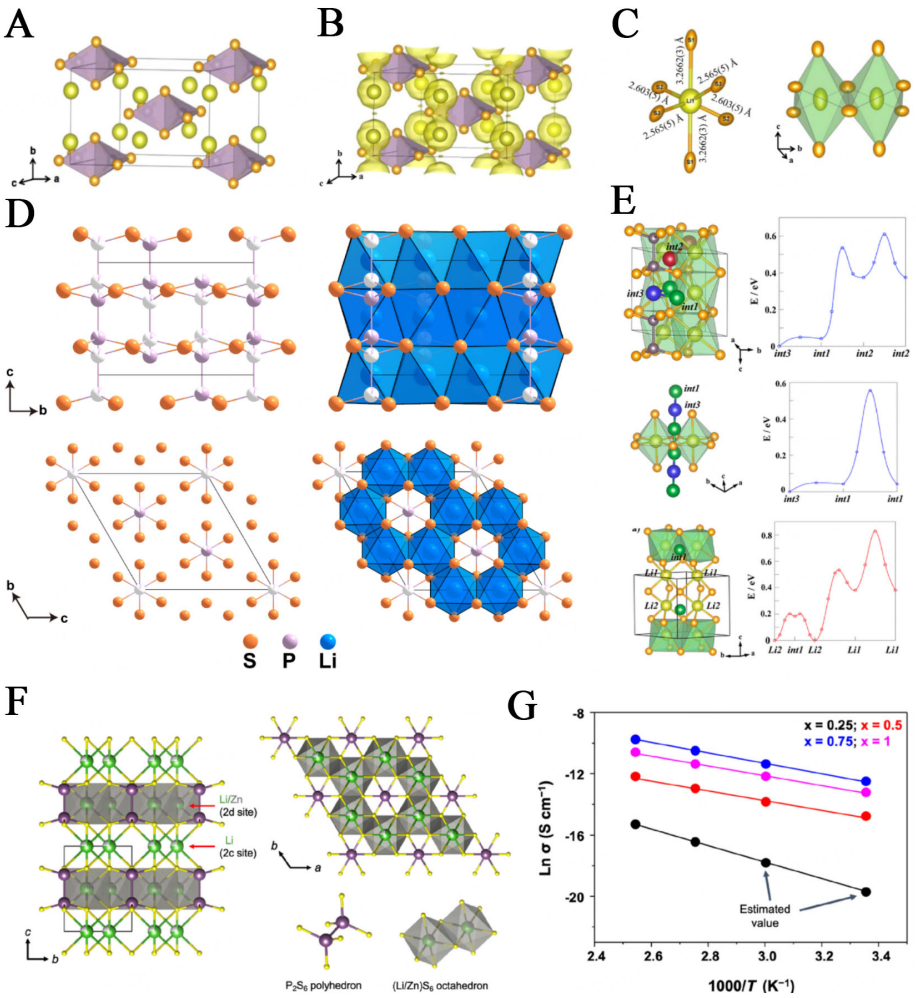

Figure 4. (A) Crystal structure of $Li_2P_2S_6$ and (B) reconstructed negative nuclear density map; (C) (left) Distorted LiS_6 octahedron and (right) edge-shared Li polyhedra along the *b*-axis in $Li_2P_2S_6$[89]. Reproduced with permission[89]. Copyright 2017, American Chemical Society; (D) Crystal structure of $Li_4P_2S_6$, projections along the *a*-, *c*-axis and perspective view emphasizing the $P_2S_6^{4-}$ and LiS_6 units[99]; (E) Diffusion pathways of $Li_4P_2S_6$ involving all three (upper) or two (middle) possible interstitial sites and vacancy-mediated diffusion (lower) between the lattice Li sites[93]. Reproduced with permission[93]. Copyright 2016, American Chemical Society; (F) Crystal structure of $Li_{4-2x}Zn_xP_2S_6$, viewed along [100], [001] (g) Arrhenius plots of the ionic conductivities for the $Li_{4-2x}Zn_xP_2S_6$ ($0.25 \leq x \leq 1$, nominal composition)[100]. Reproduced with permission[100]. Copyright 2023, Elsevier.

The crystal structure of $Li_4P_2S_6$ has been reported to have various symmetries; however, it is consistently described as a rigid framework composed of ethane-like $P_2S_6^{4-}$ building units (P^{4+}) featuring P-P bonds [Figure 4D][92,93,102-104]. The finalized crystal structure of $Li_4P_2S_6$ can be described by either *P*321 (no. 150) or $P\bar{3}m1$ (no. 164) space groups, which are almost identical to each other because their symmetry operations are related by a group-subgroup relationship. The specific equivalent sites of P in a unit cell may become disordered because the crystallization of the material is not guided by covalent bonds beyond the P-S bonds, which causes a highly disordered nature of the resulting structure[99]. The sulfur anions were packed in hexagonal *hcp* stacking, with the lithium ions occupying the octahedral sites, and formed a 3D honeycomb-like structure when viewed along the *c*-axis. Although the crystalline structure of $Li_4P_2S_6$ featured highly connected lithium-ion diffusion pathways, the material exhibited a poor ionic conductivity of 1.6×10^{-10} S cm^{-1} at room temperature, with an activation energy of 0.48 eV. Figure 4E shows the crystal structure and energy landscape diagrams of the lithium-ion diffusion pathways in $Li_4P_2S_6$, which were

mediated through interstitial or vacant sites. The diffusion process faced a higher activation barrier because of the need to pass through two fully occupied LiS_6 octahedra, which are less likely to participate in diffusion. However, diffusion along the int3-int1 and int2-int2 pathways showed a negligible barrier. Therefore, lowering the int1-int2 or Li2-Li1 barrier energy can further facilitate lithium-ion mobility within the crystal structure. Lyoo *et al.* achieved a reduction in the overall activation energy and enhanced lithium-ion conductivity in the $Li_4P_2S_6$ crystal structure by introducing vacancies by substituting Zn^{2+} for Li^+, the nominal composition of $Li_{4-2x}Zn_xP_2S_6$ ($0.25 \leq x \leq 1$) [Figure 4F][100]. A four-order-of-magnitude increase in ionic conductivity (3.8×10^{-6} S cm^{-1} at room temperature) and lowered activation energy (0.30 eV) were observed at $x = 0.75$ [Figure 4G]. These enhancements in diffusion properties were primarily attributed to the vacancies created by the Zn^{2+} ions occupying specific sites, which facilitated lithium-ion diffusion through two-dimensional (2D) *ab* planes through the lithium-ion-deficient, edge-sharing LiS_6 octahedra. However, exceeding $x = 0.75$ resulted in decreased ionic conductivity, which indicates that regulating the optimum defect concentration within the crystal structure of $Li_4P_2S_6$ is crucial.

Glass-ceramic $Li_7P_3S_{11}$ was first discovered by Mizuno *et al.* and it exhibited a high ionic conductivity of 3.2×10^{-3} S cm^{-1} at room temperature, along with a notably low activation energy of 0.19 eV[105] [Figure 5A and B]. The glassy compound $70Li_2S$-$30P_2S_5$ demonstrated lower ionic conductivity (5.4×10^{-5} S cm^{-1} at room temperature) and higher activation energy (0.39 eV) than crystalline $Li_7P_3S_{11}$[105], which demonstrates the importance of exploring suitable framework structures for lithium-ion conductors. Interestingly, crystalline $Li_7P_3S_{11}$ cannot be prepared directly through solid-state synthesis, and can only be obtained through crystallization from glass[105]. The crystal structure of $Li_7P_3S_{11}$ is described in the triclinic space group $P\bar{1}$ (no. 2), which is similar to the crystal structure of α-$Ag_7P_3S_{11}$[109]. It features corner-sharing $P_2S_7^{4-}$ ditetrahedral and isolated PS_4^{3-} units with lithium ions occupying the interstices within its structure[90,110] [Figure 5C]. The framework closely resembles a *bcc*-like anion structure, which has been proposed to significantly reduce the activation energy within the diffusion channel surrounding the lithium ions[55]. Furthermore, the flexible motion of the $P_2S_7^{4-}$ ditetrahedral units, as revealed by combined synchrotron X-ray, time-of-flight neutron diffraction, and NMR analyses, facilitated lithium-ion diffusion by flattening the energy landscape and widening the diffusion pathways[107,111,112] [Figure 5D]. Computational investigation supporting the 3D lithium-ion diffusion pathways with lithium-ion sites appeared to be disordered within the diffusion channels provided by the readily mobile $P_2S_7^{4-}$ anion species. In addition to the computational results, Chang *et al.* found that lithium diffusivity was not significantly affected by the presence of excessive defects or lithium ions, which implies that compositional tuning strategies may not be effective in enhancing the ionic conductivity of $Li_7P_3S_{11}$[108] [Figure 5E]. Overall, the framework consisting of $P_2S_7^{4-}$ ditetrahedral units and isolated PS_4^{3-} units created a flattened energy landscape for lithium-ion diffusion, making it a desirable structure for lithium-ion conductors[113].

Thio-LISICONs

The term "LISICON" was originally used to describe the oxide-based lithium-ion conductors[114]. The resulting compounds by replacing the oxygen with sulfur in LISICON are referred to as thio-LISICON[115]. Thio-LISICONs are generally represented by Li_xMS_4 (where M = Al, Si, P, Ga, Ge, Sn, or Sb). These compounds feature sulfide anions arranged in a *hcp* structure with minimal distortion and typically consist of isolated MS_4 tetrahedral frameworks with Li ions occupying the vacant sites within the framework. These lithium ions were coordinated within the LiS_4 or LiS_6 polyhedra[43,115]. The ionic conductivity of thio-LISICONs ranges from 10^{-7} to 10^{-4} S cm^{-1} at room temperature and is primarily influenced by variations in the crystal structure owing to different heat-treatment conditions or chemical tuning within the structure[26,27,41,69,116,117]. Variations in the crystal structure were particularly evident in the different stacking arrangements of the isolated MS_4 tetrahedral networks. These arrangements create distinct lithium-ion

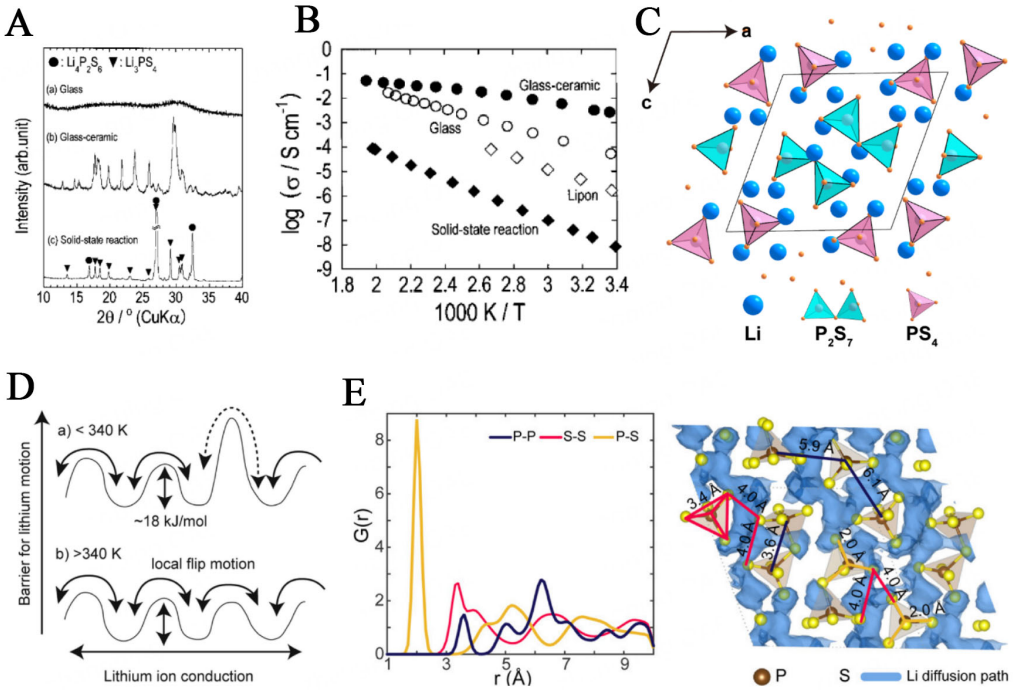

Figure 5. (A) X-ray diffraction (XRD) patterns and (B) Arrhenius plots of ionic conductivities of the $70Li_2S$-$30P_2S_5$ glasses with different synthetic conditions[105]. Reproduced with permission[105]. Copyright 2005, Wiley-VCH GmbH; (C) The crystal structure of $Li_7P_3S_{11}$[106]; (D) Schematic illustration of lithium-ion conduction and local flip motion in $Li_7P_3S_{11}$[107] Reproduced with permission[107]. Copyright 2015, American Chemical Society; (E) (left) Pair distribution function, *G*(*r*), obtained from the AIMD calculation and (right) corresponding pair schematics with lithium-ion diffusion pathways[108] Reproduced with permission[108]. Copyright 2018, American Chemical Society. AIMD: Ab initio molecular dynamics.

diffusion pathways, which cause the varied ion-conducting behaviors of the structures[118,119].

The most well-known polymorph is the Li_3PS_4 system, which exhibits three temperature-dependent phases: the high-temperature (HT) phase [*Cmcm* (no. 63) or $P2_1/m$ (no. 11), α-Li_3PS_4], the intermediate-temperature phase [*Pnma* (no. 62), β-Li_3PS_4], and the low-temperature (LT) phase [$Pmn2_1$ (no. 31), γ-Li_3PS_4]. The ionic conductivities at room temperature for the three phases are as follows: 10^{-7} S cm^{-1} for γ-Li_3PS_4[27,120], 10^{-4} S cm^{-1} for β-Li_3PS_4[26], and 1 mS cm^{-1} for α-Li_3PS_4[69]. They primarily differed in the orientation of the PS_4^{3-} tetrahedra, as shown in Figure 6A and B. Owing to the low ionic conductivity of the γ-Li_3PS_4 phase, stabilizing the crystal structure of the β- or α-Li_3PS_4 phases is important to achieve a high-performance lithium-ion conductor. Liu *et al.* stabilized β- Li_3PS_4 by fabricating it with tetrahydrofuran (THF)[26]. When THF was removed, pure nanoporous β- Li_3PS_4 was obtained, which exhibited a high ionic conductivity of 1.6×10^{-4} S cm^{-1} at room temperature and an activation energy of 0.36 eV. Furthermore, Kimura *et al.* stabilized the α-Li_3PS_4 at room temperature by rapidly heating the Li_3PS_4 glass and achieved a high ionic conductivity of 1.3×10^{-3} S cm^{-1} and an activation energy of 0.33 eV[69]. Alternatively, chemical tuning can be used to stabilize the β-type crystal structure. Zhou *et al.* achieved this by introducing Si^{4+} ions instead of P^{5+} ions, which resulted in a high ionic conductivity of 1.22 mS cm^{-1} at room temperature for a nominal composition of $Li_{3.25}Si_{0.25}P_{0.75}S_4$[116].

Recent studies suggest that the key factor contributing to the difference in ionic conductivities among the three phases was the arrangement of sulfur anions in the substructures. The α-Li_3PS_4 phase exhibited *bcc*-like sublattices, which enabled facile 3D diffusion pathways, in contrast to the β- and γ-Li_3PS_4 phases

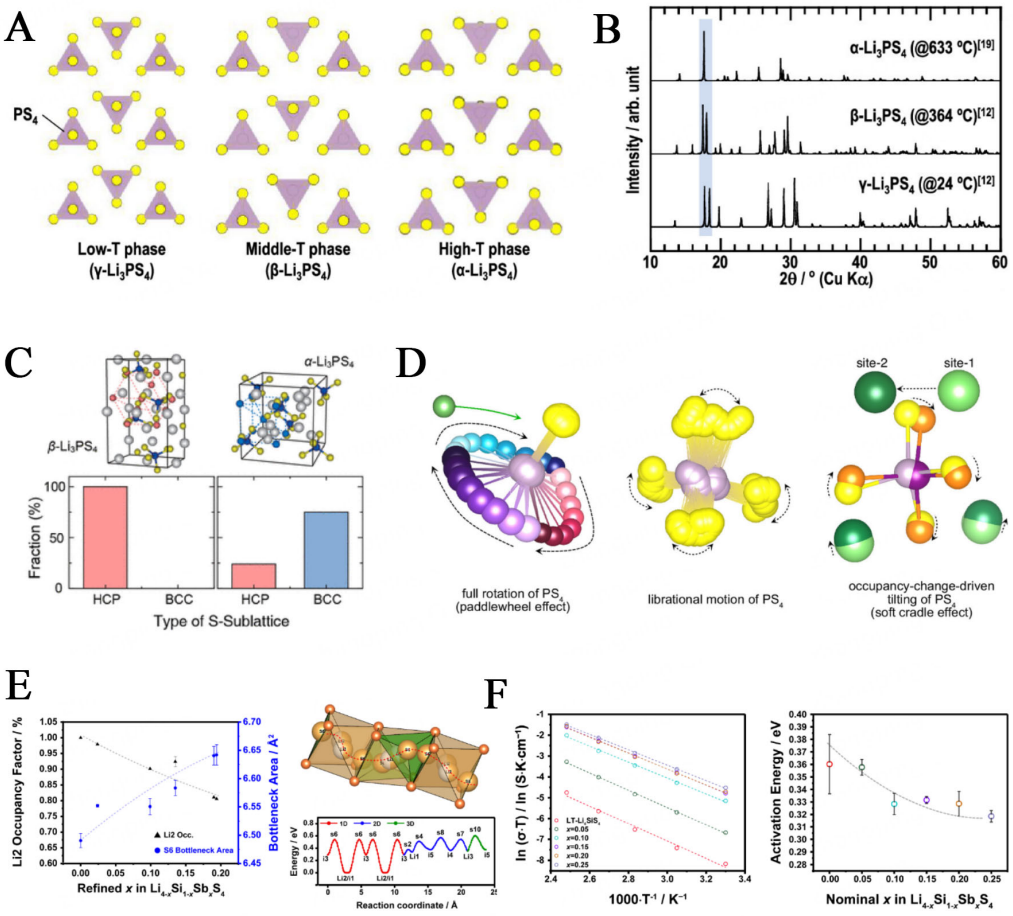

Figure 6. (A) Three different polymorphs and (B) corresponding simulated XRD patterns of Li_3PS_4[69]. Reproduced with permission[69]. Copyright 2023, American Chemical Society; (C) Fraction of stacking type of anion-sublattice in β- (left) and α-Li_3PS_4 (right)[121]. Reproduced with permission[121]. Copyright 2018, American Chemical Society; (D) Three types of rotational motion of PS_4 (left: threefold rotation, middle: librational motion, right: occupancy-change-driven tilting)[122]. Reproduced with permission[122]. Copyright 2024, Proceedings of the National Academy of Sciences; (E) (left) Lithium occupancy factor and bottleneck area as a function of x in $Li_{4-x}Si_{1-x}Sb_xS_4$ ($0 \le x \le 0.25$), and (right) 1D diffusion pathways of lithium-ion diffusion pathways with the corresponding LT-Li_4SiS_4 crystal structure; (F) (left) Arrhenius plots of ionic conductivities and (right) activation energy versus nominal composition for the $Li_{4-x}Si_{1-x}Sb_xS_4$ substitution series ($0 \le x \le 0.25$)[41]. Reproduced with permission[41]. Copyright 2024, American Chemical Society.

[Figure 6C][118,121]. While the "paddlewheel effect" has been widely accepted in the literature as an explanation for the high lithium-ion diffusion within the crystal structure of β- and α-Li_3PS_4 phases[123,124]. Jun *et al.* have recently proposed that this effect does not actually exist or contribute to the high lithium-ion diffusion[122]. Instead, they discovered that topologically isolated PS_4^{3-} units, with their tilting driven by changes in the lithium site occupancy, facilitated lithium-ion diffusion. This phenomenon has been termed the "soft-cradle effect" [Figure 6D][122].

On the other hand, the polymorph of Li_4SiS_4 exhibits a structure type similar to that of β- (LT phase) or α-Li_3PS_4 (HT phase), depending on the synthesis temperature. Unlike the Li_3PS_4 system, Li_4SiS_4 does not show a significant variation in the ionic conductivities between these different crystal structures (LT-Li_4SiS_4: 9.36×10^{-7} S cm^{-1}; HT-Li_4SiS_4: 5.25×10^{-7} S cm^{-1} at room temperature). We demonstrated significantly enhanced lithium-ion mobility by introducing defects into the crystal structure of $Li_{4-x}Si_{1-x}Sb_xS_4$ ($0 \le x \le 0.25$). An improved ionic conductivity was observed at $x = 0.15$, with a value of 3.14×10^{-5} S cm^{-1} at room temperature. This enhanced conductivity was primarily attributed to the increased bottleneck area for

lithium-ion diffusion and the formation of lithium vacancies [Figure 6E and F][41].

Li_xMS_3 (M = Si, Ge, Sn)

Li_xMS_3 includes glass ceramics such as $Li_2P_2S_6$ and $Li_4P_2S_6$[89,93], and several materials containing tetravalent cations such as Li_2SiS_3, Li_2GeS_3, and Li_2SnS_3[25,46,71,73,125]. Unlike Li_xMS_4, each element in the polyanion exhibits a distinct crystal structure with different space groups that are not related to one another. Based on the stoichiometric composition of Li_xMS_3, MS_4^{y-} tetrahedra in the structure should not be isolated. Instead, these tetrahedra were either corner-shared or formed edge-sharing $M_2S_6^{y-}$ tetrahedra. Ahn *et al.* first reported the crystal structure of Li_2SiS_3 as an orthorhombic phase of $Cmc2_1$ (No. 36) in 1989[46]. The structure comprised SiS_4^{4-} tetrahedra that were corner-shared with each other and formed infinite zigzag chains along the *c*-axis [Figure 7A]. Lithium ions occupied the tetrahedral interstices, where the LiS_4 tetrahedra were corner-shared in all directions within a unit cell. The low ionic conductivity observed for this crystal structure (2×10^{-6} S cm^{-1} at room temperature) was primarily attributed to the ordered arrangement of lithium ions within a unit cell[25,46]. Huang *et al.* chemically modified Li_2SiS_3 by introducing small amounts of phosphorus (P)[25]. They analyzed the resulting crystal structure, which featured an edge-shared dimer of the $(Si/P)_2S_6$ framework. This modification achieved a high ionic conductivity of 2.4 mS cm^{-1} at room temperature. The key advancement in the ionic conductivity is the flattened energy landscape of the interstitial lithium ions created by the edge-shared $(Si/P)_2S_6$ framework, which introduces partially occupied lithium-ion sites within a unit cell [Figure 7B and C][25].

Recently, we determined that the crystal structure of Li_2GeS_3 exhibited a $P6_1$ (no. 169) space group. The structure featured infinitely shared corners of GeS_4 tetrahedra aligned along the *c*-axis of a unit cell, which formed a spiral GeS_4 framework. The lithium ions were located within the tetrahedral interstitial sites [Figure 7D]. Favorable lithium-ion connectivity was observed through one-dimensional (1D) pathways, which were interconnected to form 3D diffusion pathways within the crystal structure [Figure 7E]. However, the structure exhibited low ionic conductivity (1.63×10^{-8} S cm^{-1} at 303 K) and an activation energy of 0.37 eV, which may be because of the ordered arrangement of lithium ions within a unit cell, as no vacant sites were available for additional lithium-ion hopping. In this context, the aliovalent anion substitution series $Li_{2-x}GeS_{3-x}Cl_x$ (x = 0.15) was designed to introduce vacancies into the crystal structure. This resulted in a tenfold increase in the ionic conductivity (1.15×10^{-7} S cm^{-1} at 303 K), and confirmed the effectiveness of the structural engineering approach in enhancing lithium-ion transport properties[71].

The crystal structure of Li_2SnS_3 was first reported by Kuhn *et al.*, and was described as crystallizing in the monoclinic space group $C2/c$ (no.15)[125]. The structure exhibited a layered configuration characterized by a partial disorder in the Li/Sn sublattice. This disorder varied depending on the synthesis conditions. For example, melt-quenched Li_2SnS_3 exhibited significant Li/Sn disorder, which resulted in an average rhombohedral structure with higher symmetry and a smaller unit cell ($R\bar{3}m$, no. 166). In contrast, a slower heating/cooling ramp rate generated a more ordered arrangement of Li and Sn in a unit cell. The relatively high ionic conductivity observed at room temperature for Li_2SnS_3 (1.5×10^{-5} S cm^{-1}) primarily originated from the 2D diffusion pathways in the *ab* plane within a unit cell, which were formed by the alternatively stacked honeycomb-like $[SnS_3]^{2-}$ layers [Figure 7F]. The ionic conductivity of this structure may be enhanced by introducing vacancies, which could promote the formation of 3D diffusion pathways or facilitate the concentrated migration of lithium ions within a unit cell. These modifications are expected to further improve the ionic conductivity.

Overall, the high ionic conductivities of thio-LISICON compounds depend on several factors. Key strategies include stabilizing the high-conductivity polymorphs, introducing vacancies to create sites for lithium-ion

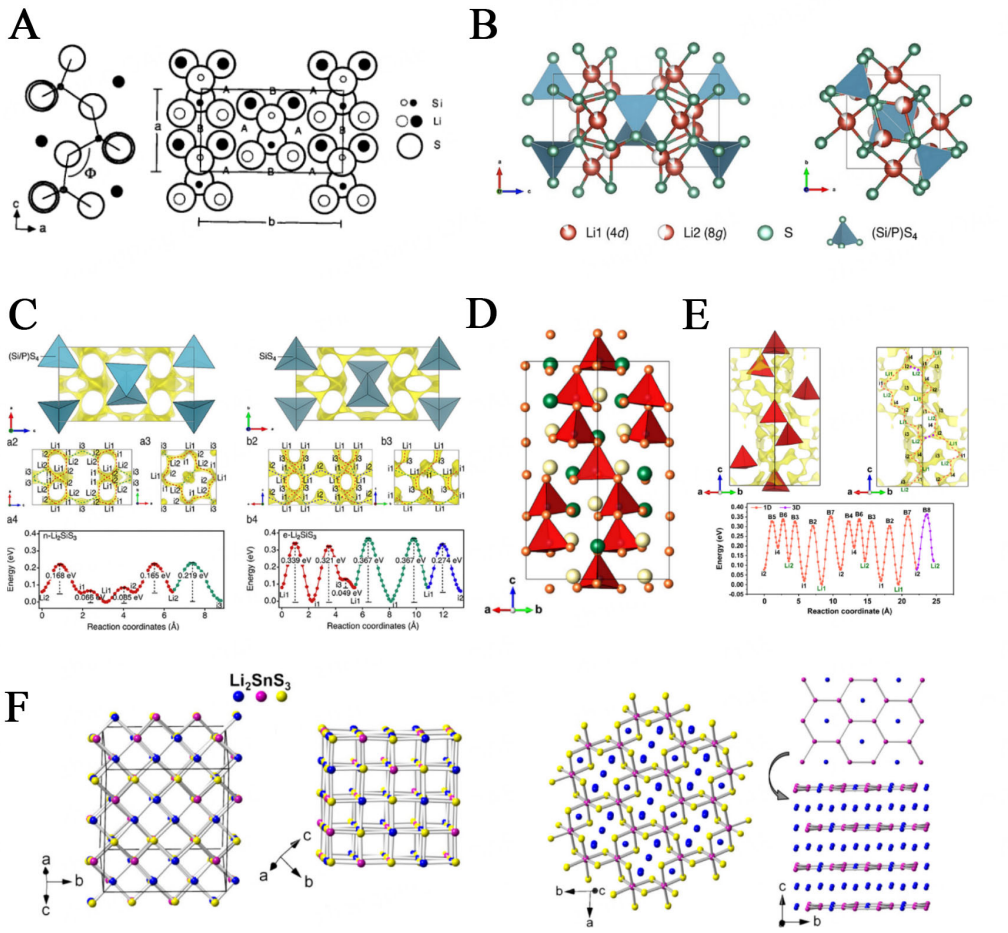

Figure 7. (A) Schematic crystal structure of orthorhombic-Li_2SiS_3[46]. Reproduced with permission[46]. Copyright 1989, Elsevier; (B) Crystal structure of tetragonal $Li_{1.82}SiP_{0.036}S_3$ viewed along the [010] and [001] directions, respectively; (C) Bond valence energy landscape calculations for lithium-ion diffusion pathways within $Li_{1.82}SiP_{0.036}S_3$ (left) and orthorhombic Li_2SiS_3 (right)[25]. Reproduced with permission[25]. Copyright 2022, American Chemical Society; (D) Crystal structure of Li_2GeS_3 and (E) corresponding lithium-ion diffusion pathways and energy diagram, as calculated by the bond valence energy landscape[71] Reproduced with permission[71]. Copyright 2023, American Chemical Society; (F) The crystal structure of Li_2SnS_3, which illustrates various projections to highlight the Sn-S framework[73]. Reproduced with permission[73]. Copyright 2015, American Chemical Society.

hopping, and leveraging diffusion mechanisms such as the soft-cradle effect to enhance lithium-ion mobility. These strategies emphasize the importance of controlling the charge-carrier concentrations in the development of high-performance ionic conductors. The effective management of these factors is crucial for advancing lithium-ion conductors in thio-LISICON systems.

Li_6PS_5X (X = Cl, Br, and I) argyrodite

The argyrodite structure was first identified in 1885 with the discovery of Ag_8GeS_6[126]. This crystal structure was characterized by highly disordered silver ions within a unit cell. Additionally, Cu can be substituted for Ag in argyrodites, and both Ag- and Cu-containing argyrodites exhibited high ionic conductivity[127-131]. The general composition of argyrodites is: $A^{m+}_{(12-n-x)/m}B^{n+}Y^{2-}_6$, where A = Li, Ag, Cu; B = Ge, Sn, P, As; Y = S, Se, Te; and $0 \le x \le 1$, where m and n represent the valence states of the cations. Inspired by the similar ionic radii of Cu^+ and Li^+, Deiseroth *et al.* proposed "Li-argyrodites", with a general structure of Li_7MS_6 or Li_6MS_5X (M = P, As, and X = Cl, Br, I)[23,132]. This argyrodite structure exhibited polymorphic behavior. The HT phase had a consistent cubic symmetry of $F\bar{4}3m$ (no. 216), regardless of the composition, whereas the

LT phase displayed either orthorhombic or monoclinic symmetries, depending on the specific composition[131]. The LT polymorph of Li_7PS_6 typically exhibits a low ionic conductivity at room temperature, whereas a high ionic conductivity is only observed in the HT cubic phase[132]. The well-known Li_6PS_5X (X = Cl, Br, I) exhibits the HT cubic phase, and each composition is characterized by varying the lattice parameters and ionic conductivity properties[36,131,132].

Figure 8A shows the crystal structure of HT-argyrodite with Li_6PS_5X (X = Cl, Br, or I). In the tetrahedral close packing of the anions, there were 136 tetrahedral sites per unit cell (Z = 4). Among these, four tetrahedral sites were occupied by P. The remaining 132 tetrahedral sites were available to accommodate the 24 lithium ions and were classified into five types based on their orientation relative to the PS_4^{3-} tetrahedra [Figure 8B]. Typically, 24 lithium ions occupy type 5/5a or type 2 tetrahedral sites. Type 5a sites were arranged in a trigonal planar configuration at the shared face between two type 5 tetrahedra. These lithium ions were disordered across equivalent positions, which formed a cage-like network. The cages were located at the tetrahedral sites within a cubic close-packed unit cell and aligned in a mirror relationship along the (110) plane. The cages exhibited a zigzag stacking pattern relative to the isotropic axes of a unit cell. Interestingly, it was observed that the X^- and S^{2-} anions occupied distinct crystallographic sites within a unit cell, with X^- forming a close-packed cubic lattice. However, anion disorder between X^- and S^{2-} (1.84 Å) occurred when their ionic radii were similar. The degree of X^-/S^{2-} anion disorder depends on the ionic radius of X^-, with the strength of disorder following the trend: Cl^- (1.81 Å) > Br^- (1.96 Å) > I^- (2.2 Å)[23,134]. The ionic conductivities of Li_6PS_5Cl, Li_6PS_5Br, and Li_6PS_5I are 1.4×10^{-3} S cm^{-1}, 8.7×10^{-3} S cm^{-1}, and 1.3×10^{-7} S cm^{-1}, respectively, at room temperature[36].

The ionic conductivity of the argyrodite structure is widely recognized to depend on four key factors: (1) Li-ion concentration[24,77,79,135], (2) unit cell volume[36,135,136], (3) degree of anion or cation site disorder[135,137-139], and (4) anion polarizability[36,136]. The disordered state of lithium ions within the cages indicates that diffusion within the cage occurs at a faster rate than diffusion between cages. Therefore, these factors must be considered in relation to the specific crystal structure because the connectivity of Li cages significantly affects the lithium-ion transport properties[140].

For instance, Li_6PS_5Cl exhibits a smaller unit cell volume than Br- or I-based argyrodites, which results in a shorter distance between the Li cages within a unit cell. This structure facilitates a high ionic conductivity of ~1 mS cm^{-1} at room temperature, along with a low activation energy[36,76,77]. The diffusion of lithium ions easily occurs between these Li cages, which facilitates control of the lithium-ion concentration or the induction of greater anion disorder, which is crucial for further enhancement of the ionic conductivity. Adeli *et al.* demonstrated that a Cl-rich argyrodite (with the nominal composition series $Li_{6-x}PS_{5-x}Cl_{1+x}$, $x \leq 0.5$) introduced more lithium-ion vacancies and greater anion disordering with Cl^-/S^{2-} within a unit cell of Li_6PS_5Cl, which resulted in an ionic conductivity of 9.4 mS cm^{-1} at room temperature, which is nine times higher than that of the original Li_6PS_5Cl [Figure 8C][77]. Because the Li cages in the crystal structure already exhibited good connectivity, introducing vacancies and increasing the monovalent Cl- anion content enhanced the diffusivity and lowered the activation energy, thereby improving the ionic conductivity of the Cl-rich argyrodite.

In the case of Li_6PS_5I, different strategies should be applied to enhance ionic conductivity. Owing to the large volume of the unit cell, the distance between the Li cages was greater than that in Li_6PS_5Cl[36]. Consequently, concerted migration could not occur along long-range diffusion between cages because of the deficiency of lithium ions within the cell. This resulted in a lower ionic conductivity and higher activation energy than those of Li_6PS_5Cl, despite their similar crystal structures[135,139,141]. Therefore, the

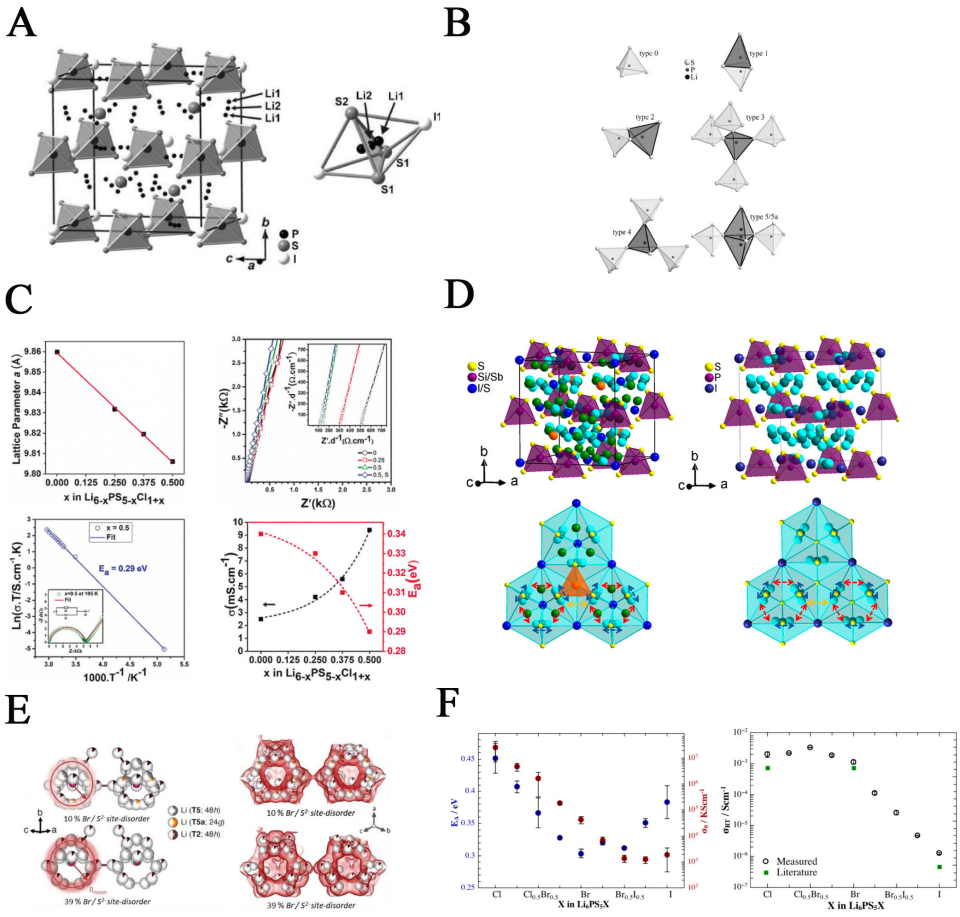

Figure 8. (A) (left) The crystal structure of Li_6PS_5I. (right) A face-shared S_3I_2 double tetrahedron with two distinct lithium-ion equivalent sites[23]. Reproduced with permission[23]. Copyright 2008, Wiley-VCH GmbH; (B) A simplified tetrahedron type in the argyrodite structure, where light gray represents PS_4 groups (type 0) and dark gray indicates lithium-containing tetrahedron types (types 1-5)[131]. Reproduced with permission[131]. Copyright 2010, Wiley-VCH GmbH; (C) (upper left) Lattice parameters of $Li_{6-x}PS_{5-x}Cl_{1+x}$ as a function of *x*. (upper right) Impedance plots at room temperature of Li_6PS_5Cl, $Li_{5.75}PS_{4.75}Cl_{1.25}$, $Li_{5.5}PS_{4.5}Cl_{1.5}$, and a sintered $Li_{5.5}PS_{4.5}Cl_{1.5}$. (lower left) Nyquist and Arrhenius plots for $Li_{5.5}PS_{4.5}Cl_{1.5}$. (lower right) Ionic conductivity and activation energy for $Li_{6-x}PS_{5-x}Cl_{1+x}$ (x = 0, 0.25, 0.375, 0.5)[77]. Reproduced with permission[77]. Copyright 2019, Wiley-VCH GmbH; (D) (upper left) Crystal structure of $Li_{6.7}Si_{0.7}Sb_{0.3}S_5I$. (lower left) Three distinct lithium ion diffusion pathways: the doublet jump (blue arrow), the intra-cage jump (red arrow), and the inter-cage jump (orange arrow). (upper right and lower left) The crystal structure of Li_6PS_5I is shown for comparison, with no additional lithium ions in the structure[24]. Reproduced with permission[24]. Copyright 2019, American Chemical Society; (E) (left) Two distinct lithium-ion cages, defined by their radius from isolated S^{2-} ions, are influenced by the Br^-/S^{2-} site disorder, and corresponding (right) lithium-ion diffusion pathways[133]. Reproduced with permission[133]. Copyright 2021, Wiley-VCH GmbH; (F) (left) The activation energy and Arrhenius prefactor as functions of X in Li_6PS_5X (X = Cl, Br, I). (right) The ionic conductivity as a function of X in Li_6PS_5X (X = Cl, Br, I)[36]. Reproduced with permission[36]. Copyright 2017, American Chemical Society.

introduction of interstitial lithium ions is an effective approach for activating 3D lithium-ion diffusion between cages[135,137]. Ohno *et al.* and Zhou *et al.* proposed a Li-rich substitution series of $Li_{6+x}M_x(P/Sb)_{1-x}S_5I$ (M = Si, Ge, Sn), which demonstrated a high ionic conductivity of up to 24 mS cm^{-1} at room temperature and a low activation energy [Figure 8D][24,139]. The enhanced ionic conductivity can be attributed to the more disordered arrangement of lithium ions, which occupied not only type 5 equivalent sites but also type 2 sites, further boosting the connectivity between the Li-ion cages and activating concerted migration within the unit cell.

Moreover, anion disorder can influence ionic conductivity by altering the local charge distribution, which subsequently affects the arrangement of lithium ions[133,137]. Gautam *et al.* analyzed the crystal structure of Li_6PS_5Br by varying the degree of Br^-/S^{2-} disorder and adjusting the cooling rates of the samples. They found that higher cooling rates resulted in a higher degree of Br^-/S^{2-} disorder[133]. As the Br^-/S^{2-} site disorder increased, the ionic conductivity also improved. This is because the increased disorder reduced the distance between the Li ions in the T2 sites that interconnect with the Li cages [Figure 8E][133]. Morgan proposed that long-range diffusion in X^-/S^{2-} disordered configurations is more favorable for lithium-ion conduction, owing to the inhomogeneous charge distribution within a unit cell. This inhomogeneity generated disorder in the lithium ions within the argyrodites, causing the energetically equivalent interstitial sites to become more uniform and facilitating easier diffusion[137].

The polarization of the anions also affects ionic conduction. Similar to the design strategy of thio-LISICONs, more polarizable anions form weaker bonds with lithium ions, thereby lowering the activation energy barrier for lithium-ion conduction and leading to a higher ionic conductivity. Schlem *et al.* demonstrated this correlation in the argyrodite nominal substitution series $Li_6PS_{5-x}Se_xI$ ($0 \leq x \leq 5$)[136], where the incorporation of larger, more polarizable Se anions decreased the observable activation energy barrier for ionic migration, which resulted in an increase in the conductivity by approximately two orders of magnitude. The increase in the lattice volume and creation of wider diffusion pathways enhanced ionic conductivity without the disruptive effects of increased anion site disorder. This suggests that lattice softening is an effective strategy for improving the ionic conductivity of the argyrodite crystal structure[136]. However, it should be noted that lattice softening also reduces the Arrhenius prefactor, particularly the attempt frequency (ν_0), as given in Equation (4). Kraft *et al.* systematically analyzed the influence of the lattice polarizability on the ionic conductivity of Li_6PS_5X (X = Cl, Br, I) [Figure 8F][36]. They proposed that increasing the lattice volume resulted in a longer jump distance and lowered the activation energy, which in turn reduced the attempt frequency, as defined by[142]:

$$\nu_0 = \frac{1}{a_0}\sqrt{\frac{2E_a}{M_{Li}}} \tag{6}$$

where M_{Li} refers to the mass of the lithium ions. Consequently, the optimal lattice softness in the argyrodite structure, such as that in $Li_6PS_5Cl_{0.5}Br_{0.5}$, results in a balanced value of the Arrhenius prefactor and activation energy, facilitating high ionic conductivity[36].

As a result, structural engineering of argyrodites, such as controlling the lithium-ion concentration, lattice softness, and anion disorder, has proven to be an effective strategy for achieving high-performance lithium-ion conductors. By understanding lithium-ion diffusion within the unit cell and optimizing the chemical or structural properties, the conductivity can be significantly enhanced.

LGPS-type ($Li_{10}GeP_2S_{12}$) structures

The discovery of LGPS dates back to an investigation by Kanno *et al.* in 2001, which focused on the solid solution series in the Li_2S-GeS_2-P_2S_5 system[143]. The solid solution in the $Li_{4-x}Ge_{1-x}P_xS_4$ system (x = 0.75; $Li_{3.25}Ge_{0.25}P_{0.75}S_4$) exhibited notably high ionic conductivity (2.2×10^{-3} S cm^{-1} at room temperature), with XRD patterns that deviated from those of pristine Li_4GeS_4 (*Pnma*, no.62) or Li_3PS_4 ($Pmn2_1$, no.31)[143]. The crystal structure of LGPS with the $P4_2/nmc$ (no. 137) space group was first reported in 2011[12]. It featured a 1D lithium-ion conduction pathway and exhibited exceptionally high bulk-ionic conductivity of over 10 mS cm^{-1} at room temperature, comparable to that of organic liquid electrolytes used in LIB systems. The framework of the unit cell comprises two equivalent tetrahedral sites: a 4*d* site with a 1:1 partial occupancy of Ge and P and a 2*d* site exclusively occupied by P, which formed an isolated MS_4 (M = Ge, P) tetrahedra.

Furthermore, single-crystal X-ray structural analysis revealed four equivalent lithium-ion sites: two LiS_4 sites that were edge-shared with each other (Li1 and Li3), which formed four channels along the *c*-axis; one LiS_6 octahedron (Li2); and a four-fold coordinated site located between the four channels along the *c*-axis (Li4)[144]. The thermal ellipsoids of Li1 and Li3 were roughly aligned along the *c*-axis, which indicates diffusion channels in this direction. In contrast, the thermal ellipsoid of Li4 was aligned perpendicularly to the *c*-axis, suggesting that it formed 3D diffusion pathways connecting the channels along the *c*-axis. Notably, Li2 exhibited smaller thermal ellipsoids, indicating inactive diffusion pathways within the unit cell. The partially occupied Li ions within the unit cell further support the unusually high ionic conductivity of LGPS [Figure 9A].

The crystal structure of the LGPS-type material comprises an S^{2-} sublattice, which is packed more akin to a *bcc* structure, unlike the *hcp*-packed structure observed in thio-LISICONs. The ideal *bcc* framework provides a continuous, face-sharing tetrahedral pathway with lower activation energy than the *hcp* or *fcc* structures [Figure 9B][55]. Therefore, the unusually high ionic conductivity of the LGPS-type structure can be attributed to (1) the ideal *bcc* framework, where the flattened energy landscape throughout the lattice promotes disordered lithium-ion distribution within a unit cell, and (2) the connectivity of lithium-ion diffusion pathways, enabling 1D and 3D network diffusion.

Bron *et al.* identified the crystal structure of $Li_{10}SnP_2S_{12}$[37], which had the same LGPS-type structure as that of LGPS [Figure 9C]. This new compound exhibited an ionic conductivity of approximately 4 mS cm^{-1} at room temperature, slightly lower than that of LGPS. Culver *et al.* studied the inductive effect in a solid-solution system of $Li_{10}Ge_{1-x}Sn_xP_2S_{12}$ to explain the reduction in the ionic conductivity despite the substitution of the more polarizable Sn for Ge[146]. They found that substituting Ge with Sn weakened the {Ge, Sn}-S bonding interactions and increased the charge density associated with the S^{2-} ions. This strengthened the interaction with lithium ions, which resulted in a lower ionic conductivity than that of LGPS [Figure 9D].

The highest ionic conductivity among the LGPS-type compounds reported to date is that of $Li_{9.54}[Si_{0.6}Ge_{0.4}]_{1.74}P_{1.44}S_{11.1}Br_{0.3}O_{0.6}$, which exhibits a conductivity of 32 mS cm^{-1} at room temperature[20]. The design approach utilized high-entropy materials and high polarizability with a target LGPS-type structure. A higher compositional complexity of constituent cations and anions (excluding lithium ions) with greater polarizability, facilitated increased lithium-ion conduction. This principle is illustrated in Figure 9E. The highest reported ionic conductivity demonstrates that even at 263 K, the material maintains a high ionic conductivity of 9 mS cm^{-1} at room temperature [Figure 9F].

Overall, the LGPS-type structure highlights the crucial role of the crystal architecture in achieving high ionic conductivity. The *bcc*-like framework in the LGPS-type materials facilitates continuous low-energy barrier pathways for Li-ion diffusion across both 1D and 3D networks. Further structural modifications, such as leveraging the inductive effect, enhancing lattice polarizability, or inducing high entropy within the crystal structure, can significantly enhance the ionic conductivity of the LGPS-type structures.

CONCLUSION AND OUTLOOK

Discovering novel structure-type solid electrolytes

In this review, we systematically characterized the relationship between the crystal structure and ionic conductivity, with a particular focus on SSEs. Most sulfide ionic conductors, including thio-phosphates, exhibit high ionic conductivity in the order of ~1 mS cm^{-1} at room temperature. Among the various sulfide materials, those with the LGPS-type structure have demonstrated the highest ionic conductivity reported so

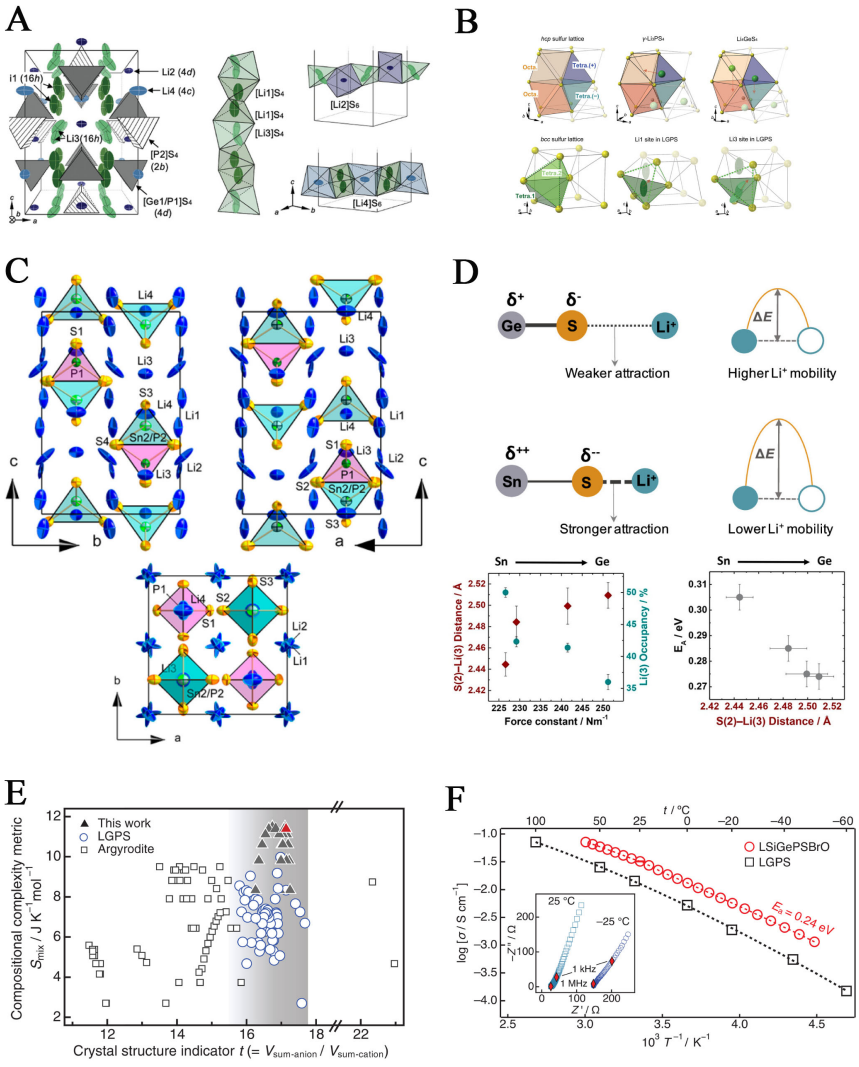

Figure 9. (A) Crystal structure of the $Li_{10}GeP_2S_{12}$; (B) Single lithium-ion jumps within the *hcp*-like packing and *bcc*-like packing of anion frameworks[145]. Reproduced with permission[145]. Copyright 2020, Wiley-VCH GmbH; (C) The crystal structure of $Li_{10}SnP_2S_{12}$[37]. Reproduced with permission[37]. Copyright 2013, American Chemical Society; (D) (upper) Schematic of the hypothetical inductive effect in M-S Li bonding for M = Ge *vs.* M = Sn. (lower left) Changes in the S-Li distances and occupancies with changing force constant in $Li_{10}Ge_{1-x}Sn_xP_2S_{12}$. (lower right) S-Li distance versus previously reported activation energies[146]. Reproduced with permission[146]. Copyright 2020, American Chemical Society; (E) Compositional complexity metric for LGPS-type and argyrodite-type versus crystal structure indicator, the volume ratio of anions to that of cations; (F) Arrhenius plots for the ionic conductivities of $Li_{9.54}[Si_{0.6}Ge_{0.4}]_{1.74}P_{1.44}S_{11.1}Br_{0.3}O_{0.6}$ and $Li_{10}GeP_2S_{12}$[20]. Reproduced with permission[20]. Copyright 2023, The American Association for the Advancement of Science.

far for solid electrolytes, which reached up to 32 mS cm^{-1} at room temperature. In the case of glass, the distribution of the framework polyanions and lithium ions is strongly influenced by the concentration of the mobile ions within the compounds. However, in crystalline compounds, lithium-ion mobility is influenced by several factors that can be optimized through structural modifications. These factors include (1) the concentration of the lithium ions, (2) structure of the lithium-ion diffusion pathways, and (3) polarizability of the crystal framework. Understanding the chemical properties of the crystal structure that affect ionic conduction, such as the soft-cradle effect, inductive effect, lattice softness, high-entropy compounds, and concerted migration mechanism within a unit cell, is essential for this purpose. To investigate the diverse crystal chemistry and enhance the superionic conduction, it is crucial to elucidate the phase-composition

relationship within previously unstudied chemical systems. This exploration may result in the discovery of new structures with high ionic conductivity.

Interfacial engineering

Although high ionic conductivity is crucial for achieving ASSBs with high energy densities, identifying a solid electrolyte that provides both excellent ionic conductivity and robust chemical and electrochemical stability remains a significant challenge. Processing sulfide compounds requires a dry-air atmosphere because of their reactivity with moisture in the air, which limits their large-scale production. Additionally, the narrow electrochemical stability window of the sulfides restricts their practical application in ASSBs, which indicates that solid electrolyte-electrode interface engineering is essential for practical deployment. The interface between the electrode and solid electrolyte during cell cycling is strongly influenced by the constituent elements of solid electrolytes, which decompose at higher or lower potentials near the electrodes. This decomposition forms stable phases composed of these elements within the interface, with their redox potential determining the interfacial stability. Therefore, doping with elements that exhibit a wide electrochemical stability window, such as halides or oxides, can enhance the interfacial stability of solid electrolytes and improve the long-term cycling performance of ASSBs.

Further studies required to develop ASSBs with the desired performance include:

(1) Hybrid Assembly of ASSBs: The intrinsically narrow electrochemical stability window of sulfides causes rapid decomposition in high-voltage regions, hindering the practical commercialization of ASSBs. Incorporating a small amount of high-voltage-stable solid electrolytes, such as halide-based solid electrolytes, in the cathode region alongside SSEs is a promising approach. This hybrid assembly can enhance long-term cycling performance by mitigating the decomposition of SSEs at high-voltage cathode regions.

(2) Exploring Nanocomposites for Anode Interfaces: ASSBs with lithium metal anodes offer high energy density but face challenges such as lithium dendrite growth during cycling, which compromises safety and degrades overall cell performance. Incorporating nanocomposite anodes with high compatibility, enhanced lithium diffusion, and stability at high currents with solid electrolytes can accelerate the commercialization of ASSBs. To advance their practical application, a more fundamental investigation into alloying and de-alloying mechanisms in nanocomposites, such as those involving silver, carbon, and silicon, is essential.

(3) Microstructure Modification: Micropores within solid electrolytes lead to contact loss at the electrode-solid electrolyte interface, necessitating improvements in the solid electrolyte's microstructure. Strategies for improvement include isostatic pressurization of the cell assembly and controlling the particle size of the solid electrolytes. Smaller particle sizes ensure larger contact areas with electrode particles and promote good contact by minimizing voids. However, a larger contact area between the solid electrolyte and electrodes may lead to increased decomposition of the solid electrolyte. Therefore, optimizing these parameters is crucial for advancing the practical application of ASSBs.

This review provides a comprehensive analysis of the crystal structures of sulfide-based solid electrolytes, serving as a valuable resource for future advancements in battery research. Continued research on highly ionic conductors is essential for deepening our understanding of ion conduction mechanisms within crystalline structures. Such insights will not only enhance the performance of the existing solid electrolytes, but also aid in the discovery of new crystal structures and chemistries.

DECLARATIONS

Authors' contributions

Conceived the manuscript: Roh, J.; Do, N.
Wrote the manuscript: Roh, J.; Do N.
Reviewed the manuscript: Hong, S. T.; Chae, M. S.
Contributed to the discussion of the manuscript: Roh, J.; Do, N.; Lee, H.; Lee, S.; Pyun, J.; Hong S. T.; Chae, M. S.

Availability of data and materials

Not applicable.

Financial support and sponsorship

This work was supported by a National Research Foundation of Korea (NRF) grant funded by the Korean government (MSIT) (No. 2020R1A2C2007070).

Conflicts of interest

All authors declared that there are no conflicts of interest.

Ethical approval and consent to participate

Not applicable.

Consent for publication

Not applicable.

REFERENCES

1. Frith, J. T.; Lacey, M. J.; Ulissi, U. A non-academic perspective on the future of lithium-based batteries. *Nat. Commun.* **2023**, *14*, 420. DOI PubMed PMC
2. Blomgren, G. E. The development and future of lithium ion batteries. *J. Electrochem. Soc.* **2017**, *164*, A5019-25. DOI
3. Jung, H.; Silva, R.; Han, M. Scaling trends of electric vehicle performance: driving range, fuel economy, peak power output, and temperature effect. *World. Electr. Veh. J.* **2018**, *9*, 46. DOI
4. Li, H. Practical evaluation of Li-ion batteries. *Joule* **2019**, *3*, 911-4. DOI
5. Cao, W.; Zhang, J.; Li, H. Batteries with high theoretical energy densities. *Energy. Storage. Mater.* **2020**, *26*, 46-55. DOI
6. USCAR. Development of advanced high-performance batteries for electric vehicle (EV) applications. Available from: https://uscar.org/publications/. [Last accessed on 28 Feb 2025].
7. Kong, L.; Li, C.; Jiang, J.; Pecht, M. G. Li-ion battery fire hazards and safety strategies. *Energies* **2018**, *11*, 2191. DOI
8. Chen, Y.; Kang, Y.; Zhao, Y.; et al. A review of lithium-ion battery safety concerns: the issues, strategies, and testing standards. *J. Energy. Chem.* **2021**, *59*, 83-99. DOI
9. Liang, Y.; Zhao, C.; Yuan, H.; et al. A review of rechargeable batteries for portable electronic devices. *InfoMat* **2019**, *1*, 6-32. DOI
10. Xu, K. Nonaqueous liquid electrolytes for lithium-based rechargeable batteries. *Chem. Rev.* **2004**, *104*, 4303-418. DOI PubMed
11. Hess, S.; Wohlfahrt-mehrens, M.; Wachtler, M. Flammability of Li-ion battery electrolytes: flash point and self-extinguishing time measurements. *J. Electrochem. Soc.* **2015**, *162*, A3084-97. DOI
12. Kamaya, N.; Homma, K.; Yamakawa, Y.; et al. A lithium superionic conductor. *Nat. Mater.* **2011**, *10*, 682-6. DOI
13. Kato, Y.; Hori, S.; Saito, T.; et al. High-power all-solid-state batteries using sulfide superionic conductors. *Nat. Energy.* **2016**, *1*, 16030. DOI
14. Swiderska-mocek, A.; Jakobczyk, P.; Rudnicka, E.; Lewandowski, A. Flammability parameters of lithium-ion battery electrolytes. *J. Mol. Liq.* **2020**, *318*, 113986. DOI
15. Stallworth, P.; Fontanella, J.; Wintersgill, M.; et al. NMR, DSC and high pressure electrical conductivity studies of liquid and hybrid electrolytes. *J. Power. Sources.* **1999**, *81-82*, 739-47. DOI
16. Cao, D.; Sun, X.; Li, Q.; Natan, A.; Xiang, P.; Zhu, H. Lithium dendrite in all-solid-state batteries: growth mechanisms, suppression strategies, and characterizations. *Matter* **2020**, *3*, 57-94. DOI

17. Sastre, J.; Futscher, M. H.; Pompizi, L.; et al. Blocking lithium dendrite growth in solid-state batteries with an ultrathin amorphous Li-La-Zr-O solid electrolyte. *Commun. Mater.* **2021**, *2*, 177. DOI
18. Jung, K.; Shin, H.; Park, M.; Lee, J. Solid-state lithium batteries: bipolar design, fabrication, and electrochemistry. *ChemElectroChem* **2019**, *6*, 3842-59. DOI
19. Tan, D. H.; Meng, Y. S.; Jang, J. Scaling up high-energy-density sulfidic solid-state batteries: a lab-to-pilot perspective. *Joule* **2022**, *6*, 1755-69. DOI
20. Li, Y.; Song, S.; Kim, H.; et al. A lithium superionic conductor for millimeter-thick battery electrode. *Science* **2023**, *381*, 50-3. DOI
21. Ohno, S.; Bernges, T.; Buchheim, J.; et al. How certain are the reported Ionic conductivities of thiophosphate-based solid electrolytes? *ACS. Energy. Lett.* **2020**, *5*, 910-5. DOI
22. Murugan, R.; Thangadurai, V.; Weppner, W. Fast lithium ion conduction in garnet-type $Li_7La_3Zr_2O_{12}$. *Angew. Chem. Int. Ed.* **2007**, *46*, 7778-81. DOI PubMed
23. Deiseroth, H. J.; Kong, S. T.; Eckert, H.; et al. Li_6PS_5X: a class of crystalline Li-rich solids with an unusually high Li^+ mobility. *Angew. Chem. Int. Ed.* **2008**, *47*, 755-8. DOI
24. Zhou, L.; Assoud, A.; Zhang, Q.; Wu, X.; Nazar, L. F. New family of argyrodite thioantimonate lithium superionic conductors. *J. Am. Chem. Soc.* **2019**, *141*, 19002-13. DOI
25. Huang, W.; Matsui, N.; Hori, S.; et al. Anomalously high ionic conductivity of Li_2SiS_3-type conductors. *J. Am. Chem. Soc.* **2022**, *144*, 4989-94. DOI
26. Liu, Z.; Fu, W.; Payzant, E. A.; et al. Anomalous high ionic conductivity of nanoporous β-Li_3PS_4. *J. Am. Chem. Soc.* **2013**, *135*, 975-8. DOI
27. Homma, K.; Yonemura, M.; Kobayashi, T.; Nagao, M.; Hirayama, M.; Kanno, R. Crystal structure and phase transitions of the lithium ionic conductor Li_3PS_4. *Solid. State. Ionics.* **2011**, *182*, 53-8. DOI
28. Lee, Y.; Jeong, J.; Lee, H. J.; et al. Lithium argyrodite sulfide electrolytes with high ionic conductivity and air stability for all-solid-state Li-ion batteries. *ACS. Energy. Lett.* **2022**, *7*, 171-9. DOI
29. Sakuda, A.; Hayashi, A.; Tatsumisago, M. Sulfide solid electrolyte with favorable mechanical property for all-solid-state lithium battery. *Sci. Rep.* **2013**, *3*, 2261. DOI PubMed PMC
30. Reddy, M. V.; Julien, C. M.; Mauger, A.; Zaghib, K. Sulfide and oxide inorganic solid electrolytes for all-solid-state Li batteries: a review. *Nanomaterials* **2020**, *10*, 1606. DOI PubMed PMC
31. Kotobuki, M.; Munakata, H.; Kanamura, K.; Sato, Y.; Yoshida, T. Compatibility of $Li_7La_3Zr_2O_{12}$ solid electrolyte to all-solid-state battery using Li metal anode. *J. Electrochem. Soc.* **2010**, *157*, A1076. DOI
32. Kim, K. H.; Iriyama, Y.; Yamamoto, K.; et al. Characterization of the interface between $LiCoO_2$ and $Li_7La_3Zr_2O_{12}$ in an all-solid-state rechargeable lithium battery. *J. Power. Sources.* **2011**, *196*, 764-7. DOI
33. Kwak, H.; Kim, J. S.; Han, D.; et al. Boosting the interfacial superionic conduction of halide solid electrolytes for all-solid-state batteries. *Nat. Commun.* **2023**, *14*, 2459. DOI PubMed PMC
34. Seino, Y.; Ota, T.; Takada, K.; Hayashi, A.; Tatsumisago, M. A sulphide lithium super ion conductor is superior to liquid ion conductors for use in rechargeable batteries. *Energy. Environ. Sci.* **2014**, *7*, 627-31. DOI
35. Kwak, H.; Han, D.; Lyoo, J.; et al. New cost-effective halide solid electrolytes for all-solid-state batteries: mechanochemically prepared Fe^{3+}-substituted Li_2ZrCl_6. *Adv. Energy. Mater.* **2021**, *11*, 2003190. DOI
36. Kraft, M. A.; Culver, S. P.; Calderon, M.; et al. Influence of lattice polarizability on the ionic conductivity in the lithium superionic argyrodites Li_6PS_5X (X = Cl, Br, I). *J. Am. Chem. Soc.* **2017**, *139*, 10909-18. DOI
37. Bron, P.; Johansson, S.; Zick, K.; Schmedt, G. J.; Dehnen, S.; Roling, B. $Li_{10}SnP_2S_{12}$: an affordable lithium superionic conductor. *J. Am. Chem. Soc.* **2013**, *135*, 15694-7. DOI PubMed
38. Takada, K.; Aotani, N.; Kondo, S. Electrochemical behaviors of Li^+ ion conductor, Li_3PO_4-Li_2S-SiS_2. *J. Power. Sources.* **1993**, *43*, 135-41. DOI
39. Basu, B.; Maiti, H. S.; Paul, A. Lithium ion conductivity in the system Li_4SiO_4-Li_3VO_4. *Trans. the. Indian. Ceram. Soc.* **1985**, *44*, 97-100. DOI
40. Lim, H.; Kim, S.; Kim, J.; Kim, Y.; Kim, S. Structure of Li_5AlS_4 and comparison with other lithium-containing metal sulfides. *J. Solid. State. Chem.* **2018**, *257*, 19-25. DOI
41. Roh, J.; Kim, H.; Lee, H.; et al. Unraveling polymorphic crystal structures of Li_4SiS_4 for all-solid-state batteries: enhanced ionic conductivity via aliovalent sb substitution. *Chem. Mater.* **2024**, *36*, 6973-84. DOI
42. Kimura, T.; Hotehama, C.; Sakuda, A.; Tatsumisago, M.; Hayashi, A. Structures and conductivities of stable and metastable Li_5GaS_4 solid electrolytes. *RSC. Adv.* **2021**, *11*, 25211-6. DOI PubMed PMC
43. Murayama, M.; Kanno, R.; Kawamoto, Y.; Kamiyama, T. Structure of the thio-LISICON, Li_4GeS_4. *Solid. State. Ionics.* **2002**, *154-155*, 789-94. DOI
44. Kaib, T.; Haddadpour, S.; Kapitein, M.; et al. New lithium chalcogenidotetrelates, LiChT: synthesis and characterization of the Li^+-conducting tetralithium *ortho*- sulfidostannate Li_4SnS_4. *Chem. Mater.* **2012**, *24*, 2211-9. DOI
45. Kimura, T.; Kato, A.; Hotehama, C.; Sakuda, A.; Hayashi, A.; Tatsumisago, M. Preparation and characterization of lithium ion conductive Li_3SbS_4 glass and glass-ceramic electrolytes. *Solid. State. Ionics.* **2019**, *333*, 45-9. DOI
46. Ahn, B. T.; Huggins, R. A. Synthesis and lithium conductivities of Li_2SiS_3 and Li_4SiS_4. *Mater. Res. Bull.* **1989**, *24*, 889-97. DOI
47. Menetrier, M.; Hojjaji, A.; Estournes, C.; Levasseur, A. Ionic conduction in the B_2S_3-Li_2S glass system. *Solid. State. Ionics.* **1991**, *48*,

325-30. DOI

48. Hayashi, A.; Fukuda, T.; Hama, S.; et al. Lithium ion conducting glasses and glass-ceramics in the systems Li_2S-M_xS_y (M=Al, Si and P) prepared by mechanical milling. *J. Ceram. Soc. Jpn.* **2004**, S695-9. DOI
49. Souquet, J.; Robinel, E.; Barrau, B.; Ribes, M. Glass formation and ionic conduction in the M_2S GeS_2 (M = Li, Na, Ag) systems. *Solid. State. Ionics.* **1981**, *3-4*, 317-21. DOI
50. Zhang, J.; Gao, C.; He, C.; et al. Effects of different glass formers on Li_2S-P_2S_5-MS_2 (M = Si, Ge, Sn) chalcogenide solid-state electrolytes. *J. Am. Ceram. Soc.* **2023**, *106*, 354-64. DOI
51. Nagamedianova, Z.; Sánchez, E. Preparation and thermal properties of novel Li_2S-Sb_2S_3 glassy system. *J. Non-Cryst. Solids.* **2002**, *311*, 1-9. DOI
52. Souquet, J. L. Ionic transport in amorphous solid electrolytes. *Annu. Rev. Mater. Sci.* **1981**, *11*, 211-31. DOI
53. Minami, K.; Hayashi, A.; Tatsumisago, M. Crystallization process for superionic $Li_7P_3S_{11}$ glass-ceramic electrolytes: superionic $Li_7P_3S_{11}$ glass-ceramic electrolytes. *J. Am. Ceram. Soc.* **2011**, *94*, 1779-83. DOI
54. Zhou, L.; Minafra, N.; Zeier, W. G.; Nazar, L. F. Innovative approaches to Li-argyrodite solid electrolytes for all-solid-state lithium batteries. *Acc. Chem. Res.* **2021**, *54*, 2717-28. DOI PubMed
55. Wang, Y.; Richards, W. D.; Ong, S. P.; et al. Design principles for solid-state lithium superionic conductors. *Nat. Mater.* **2015**, *14*, 1026-31. DOI
56. Tilley, R. J. D. Defects in solids. John Wiley & Sons; 2008. p. 1-552. DOI
57. Zhang, Q.; Cao, D.; Ma, Y.; Natan, A.; Aurora, P.; Zhu, H. Sulfide-based solid-state electrolytes: synthesis, stability, and potential for all-solid-state batteries. *Adv. Mater.* **2019**, *31*, 1901131. DOI PubMed
58. Ohno, S.; Banik, A.; Dewald, G. F.; et al. Materials design of ionic conductors for solid state batteries. *Prog. Energy.* **2020**, *2*, 022001. DOI
59. Tuller, H. L. Ceramic materials for electronics. 3th ed. Boca Raton: CRC Press; 2004. p. 692. Available from: https://doi.org/10.1201/9781315273242. [Last accessed on 28 Feb 2025].
60. Wang, C.; Xu, B. B.; Zhang, X.; et al. Ion hopping: design principles for strategies to improve ionic conductivity for inorganic solid electrolytes. *Small* **2022**, *18*, 2107064. DOI
61. Zhang, Z.; Kennedy, J. Synthesis and characterization of the B_2S_3 Li_2S, the P_2S_5 Li_2S and the B_2S_3 P_2S_5 Li_2S glass systems. *Solid. State. Ionics.* **1990**, *38*, 217-24. DOI
62. Dietrich, C.; Weber, D. A.; Sedlmaier, S. J.; et al. Lithium ion conductivity in Li_2S-P_2S_5 glasses - building units and local structure evolution during the crystallization of superionic conductors Li_3PS_4, $Li_7P_3S_{11}$ and $Li_4P_2S_7$. *J. Mater. Chem. A.* **2017**, *5*, 18111-9. DOI
63. Mercier, R.; Malugani, J.; Fahys, B.; Robert, G. Superionic conduction in Li_2S-P_2S_5-LiI- glasses. *Solid. State. Ionics.* **1981**, *5*, 663-6. DOI
64. Yamauchi, A.; Sakuda, A.; Hayashi, A.; Tatsumisago, M. Preparation and ionic conductivities of $(100 - x)(0.75Li_2S{\cdot}0.25P_2S_5){\cdot}x$LiBH$_4$ glass electrolytes. *J. Power. Sources.* **2013**, *244*, 707-10. DOI
65. Park, K. H.; Oh, D. Y.; Choi, Y. E.; et al. Solution-processable glass LiI-Li_4SnS_4 superionic conductors for all-solid-state Li-ion batteries. *Adv. Mater.* **2016**, *28*, 1874-83. DOI
66. Shao, Y.; Gao, C.; He, C.; et al. Ultra-long cycling life Li_2S-P_2S_5-B_2S_3 solid electrolyte via LiI doping. *Ceram. Int.* **2024**, *50*, 31032-9. DOI
67. Kennedy, J.; Sahami, S.; Shea, S.; Zhang, Z. Preparation and conductivity measurements of SiS_2 Li_2S glasses doped with LiBr and LiCl. *Solid. State. Ionics.* **1986**, *18-19*, 368-71. DOI
68. Hao, X.; Quirk, J. A.; Zhao, F.; et al. Regulating ion diffusion and stability in amorphous thiosilicate□based solid electrolytes through edge□sharing local structures. *Adv. Energy. Mater.* **2024**, *14*, 2304556. DOI
69. Kimura, T.; Inaoka, T.; Izawa, R.; et al. Stabilizing high-temperature α-Li_3PS_4 by rapidly heating the glass. *J. Am. Chem. Soc.* **2023**, *145*, 14466-74. DOI
70. Hori, S.; Suzuki, K.; Hirayama, M.; et al. Synthesis, structure, and ionic conductivity of solid solution, $Li_{10+\delta}M_{1+\delta}P_{2-\delta}S_{12}$ (M = Si, Sn). *Faraday. Discuss.* **2014**, *176*, 83-94. DOI
71. Roh, J.; Do, N.; Manjón-Sanz, A.; Hong, S. T. Li_2GeS_3: lithium ionic conductor with an unprecedented structural type. *Inorg. Chem.* **2023**, *62*, 15856-63. DOI PubMed
72. Taeahn, B.; Huggins, R. Phase behavior and conductivity of Li_2SiS_3 composition. *Solid. State. Ionics.* **1991**, *46*, 237-42. DOI
73. Brant, J. A.; Massi, D. M.; Holzwarth, N. A. W.; et al. Fast lithium ion conduction in Li_2SnS_3: synthesis, physicochemical characterization, and electronic structure. *Chem. Mater.* **2015**, *27*, 189-96. DOI
74. Kanno, R.; Hata, T.; Kawamoto, Y.; Irie, M. Synthesis of a new lithium ionic conductor, thio-LISICON-lithium germanium sulfide system. *Solid. State. Ionics.* **2000**, *130*, 97-104. DOI
75. Tatsumisago, M.; Mizuno, F.; Hayashi, A. All-solid-state lithium secondary batteries using sulfide-based glass-ceramic electrolytes. *J. Power. Sources.* **2006**, *159*, 193-9. DOI
76. Rao, R. P.; Adams, S. Studies of lithium argyrodite solid electrolytes for all-solid-state batteries. *Physica. Status. Solidi. (a).* **2011**, *208*, 1804-7. DOI
77. Adeli, P.; Bazak, J. D.; Park, K. H.; et al. Boosting solid-state diffusivity and conductivity in lithium superionic argyrodites by halide substitution. *Angew. Chem. Int. Ed.* **2019**, *58*, 8681-6. DOI
78. Wang, P.; Liu, H.; Patel, S.; et al. Fast ion conduction and its origin in $Li_{6-x}PS_{5-x}Br_{1+x}$. *Chem. Mater.* **2020**, *32*, 3833-40. DOI

79. Hogrefe, K.; Minafra, N.; Hanghofer, I.; Banik, A.; Zeier, W. G.; Wilkening, H. M. R. Opening diffusion pathways through site disorder: the interplay of local structure and ion dynamics in the solid electrolyte $Li_{6+x}P_{1-x}Ge_xS_5I$ as probed by neutron diffraction and NMR. *J. Am. Chem. Soc.* **2022**, *144*, 1795-812. DOI PubMed PMC
80. Warburg, E. Ueber die electrolyse des festen glases. *Ann. Phys.* **1884**, *257*, 622-46. DOI
81. Bih, L. Electronic and ionic conductivity of glasses inside the Li_2O-MoO_3-P_2O_5 system. *Solid. State. Ionics.132*, 71-85. DOI
82. Tatsumisago, M.; Yoneda, K.; Machida, N.; Hinami, T. Ionic conductivity of rapidly quenched glasses with high concentration of lithium ions. *J. Non-Cryst. Solids.* **1987**, *95-96*, 857-64. DOI
83. Rogez, J.; Knauth, P.; Garnier, A.; Ghobarkar, H.; Schäf, O. Determination of the crystallization enthalpies of lithium ion conducting alumino-silicate glasses. *J. Non-Cryst. Solids.* **2000**, *262*, 177-82. DOI
84. Ohara, K.; Mitsui, A.; Mori, M.; et al. Structural and electronic features of binary Li_2S-P_2S_5 glasses. *Sci. Rep.* **2016**, *6*, 21302. DOI PubMed PMC
85. Morimoto, H.; Yamashita, H.; Tatsumisago, M.; Minami, T. Mechanochemical synthesis of new amorphous materials of $60Li_2S{\cdot}40SiS_2$ with high lithium ion conductivity. *J. Am. Ceram. Soc.* **1999**, *82*, 1352-4. DOI
86. Jiusti, J.; Zanotto, E. D.; Feller, S. A.; et al. Effect of network formers and modifiers on the crystallization resistance of oxide glasses. *J. Non-Cryst. Solids.* **2020**, *550*, 120359. DOI
87. Lee, B.; Jun, K.; Ouyang, B.; Ceder, G. Weak correlation between the polyanion environment and ionic conductivity in amorphous Li-P-S superionic conductors. *Chem. Mater.* **2023**, *35*, 891-9. DOI
88. Hayashi, A.; Hama, S.; Minami, T.; Tatsumisago, M. Formation of superionic crystals from mechanically milled Li_2S-P_2S_5 glasses. *Electrochem. Commun.* **2003**, *5*, 111-4. DOI
89. Dietrich, C.; Weber, D. A.; Culver, S.; et al. Synthesis, structural characterization, and lithium ion conductivity of the lithium thiophosphate $Li_2P_2S_6$. *Inorg. Chem.* **2017**, *56*, 6681-7. DOI
90. Yamane, H.; Shibata, M.; Shimane, Y.; et al. Crystal structure of a superionic conductor, $Li_7P_3S_{11}$. *Solid. State. Ionics.* **2007**, *178*, 1163-7. DOI
91. Kong, S. T.; Gün, O.; Koch, B.; Deiseroth, H. J.; Eckert, H.; Reiner, C. Structural characterisation of the Li argyrodites Li_7PS_6 and Li_7PSe_6 and their solid solutions: quantification of site preferences by MAS-NMR spectroscopy. *Chemistry* **2010**, *16*, 5138-47. DOI PubMed
92. Neuberger, S.; Culver, S. P.; Eckert, H.; Zeier, W. G.; Schmedt, A. G. J. Refinement of the crystal structure of $Li_4P_2S_6$ using NMR crystallography. *Dalton. Trans.* **2018**, *47*, 11691-5. DOI PubMed
93. Dietrich, C.; Sadowski, M.; Sicolo, S.; et al. Local structural investigations, defect formation, and ionic conductivity of the lithium ionic conductor $Li_4P_2S_6$. *Chem. Mater.* **2016**, *28*, 8764-73. DOI
94. Mizuno, F.; Hayashi, A.; Tadanaga, K.; Tatsumisago, M. High lithium ion conducting glass-ceramics in the system Li_2S-P_2S_5. *Solid. State. Ionics.* **2006**, *177*, 2721-5. DOI
95. Wang, S.; Fu, J.; Liu, Y.; et al. Design principles for sodium superionic conductors. *Nat. Commun.* **2023**, *14*, 7615. DOI PubMed PMC
96. He, X.; Zhu, Y.; Mo, Y. Origin of fast ion diffusion in super-ionic conductors. *Nat. Commun.* **2017**, *8*, 15893. DOI PubMed PMC
97. Park, K. H.; Bai, Q.; Kim, D. H.; et al. Design strategies, practical considerations, and new solution processes of sulfide solid electrolytes for all□solid□state batteries. *Adv. Energy. Mater.* **2018**, *8*, 1800035. DOI
98. Bachman, J. C.; Muy, S.; Grimaud, A.; et al. Inorganic solid-state electrolytes for lithium batteries: mechanisms and properties governing ion conduction. *Chem. Rev.* **2016**, *116*, 140-62. DOI
99. Oxley, B. M.; Lee, K.; Ie, T. S.; et al. Structure, second-, and third-harmonic generation of $Li_4P_2S_6$: a wide gap material with a high laser-induced damage threshold. *Chem. Mater.* **2023**, *35*, 7322-32. DOI
100. Lyoo, J.; Kim, H. J.; Hyoung, J.; Chae, M. S.; Hong, S. Zn substituted $Li_4P_2S_6$ as a solid lithium-ion electrolyte for all-solid-state lithium batteries. *J. Solid. State. Chem.* **2023**, *320*, 123861. DOI
101. Eckert, H.; Zhang, Z.; Kennedy, J. H. Structural transformation of non-oxide chalcogenide glasses. The short-range order of lithium sulfide (Li2S)-phosphorus pentasulfide (P2S5) glasses studied by quantitative phosphorus-31, lithium-6, and lithium-7 high-resolution solid-state NMR. *Chem. Mater.* **1990**, *2*, 273-9. DOI
102. Mercier, R.; Malugani, J.; Fahys, B.; Douglande, J.; Robert, G. Synthese, structure cristalline et analyse vibrationnelle de l'hexathiohypodiphosphate de lithium $Li_4P_2S_6$. *J. Solid. State. Chem.* **1982**, *43*, 151-62. DOI
103. Hood, Z. D.; Kates, C.; Kirkham, M.; Adhikari, S.; Liang, C.; Holzwarth, N. Structural and electrolyte properties of $Li_4P_2S_6$. *Solid. State. Ionics.* **2016**, *284*, 61-70. DOI
104. Yahia H, Motohashi K, Mori S, Sakuda A, Hayashi A. Twinned single crystal structure of $Li_4P_2S_6$. *Z. Kristallogr. Cryst. Mater.* **2023**, *238*, 209-16. DOI
105. Mizuno, F.; Hayashi, A.; Tadanaga, K.; Tatsumisago, M. New, highly ion-conductive crystals precipitated from Li_2S-P_2S_5 glasses. *Adv. Mater.* **2005**, *17*, 918-21. DOI
106. Tatsumisago, M.; Nagao, M.; Hayashi, A. Recent development of sulfide solid electrolytes and interfacial modification for all-solid-state rechargeable lithium batteries. *J. Asian. Ceram. Soc.* **2013**, *1*, 17-25. DOI
107. Murakami, M.; Shimoda, K.; Shiotani, S.; et al. Dynamical origin of ionic conductivity for $Li_7P_3S_{11}$ metastable crystal as studied by $^{6/7}Li$ and ^{31}P solid-state NMR. *J. Phys. Chem. C.* **2015**, *119*, 24248-54. DOI
108. Chang, D.; Oh, K.; Kim, S. J.; Kang, K. Super-ionic conduction in solid-state $Li_7P_3S_{11}$-type sulfide electrolytes. *Chem. Mater.* **2018**,

30, 8764-70. DOI

109. Brinkmann, C.; Eckert, H.; Wilmer, D.; et al. Re-entrant phase transition of the crystalline ion conductor $Ag_7P_3S_{11}$. *Solid. State. Sci.* **2004**, *6*, 1077-88. DOI
110. Onodera, Y.; Mori, K.; Otomo, T.; et al. Crystal structure of $Li_7P_3S_{11}$ studied by neutron and synchrotron X-ray powder diffraction. *J. Phys. Soc. Jpn.* **2010**, *79*, 87-9. DOI
111. Mori, K.; Ichida, T.; Iwase, K.; et al. Visualization of conduction pathways in lithium superionic conductors: Li_2S-P_2S_5 glasses and $Li_7P_3S_{11}$ glass-ceramic. *Chem. Phys. Lett.* **2013**, *584*, 113-8. DOI
112. Mori, K.; Enjuji, K.; Murata, S.; et al. Direct observation of fast lithium-ion diffusion in a superionic conductor: $Li_7P_3S_{11}$ metastable crystal. *Phys. Rev. Applied.* **2015**, 4. DOI
113. Xiong, K.; Longo, R.; Kc, S.; Wang, W.; Cho, K. Behavior of Li defects in solid electrolyte lithium thiophosphate $Li_7P_3S_{11}$: a first principles study. *Comput. Mater. Sci.* **2014**, *90*, 44-9. DOI
114. Hong, H. Crystal structure and ionic conductivity of $Li_{14}Zn(GeO_4)4$ and other new Li^+ superionic conductors. *Mater. Res. Bull.* **1978**, *13*, 117-24. DOI
115. Tao, B.; Ren, C.; Li, H.; et al. Thio-/LISICON and LGPS-type solid electrolytes for all-solid-state lithium-ion batteries. *Adv. Funct. Mater.* **2022**, *32*, 2203551. DOI
116. Zhou, L.; Assoud, A.; Shyamsunder, A.; et al. An entropically stabilized fast-ion conductor: $Li_{3.25}[Si_{0.25}P_{0.75}]S_4$. *Chem. Mater.* **2019**, *31*, 7801-11. DOI
117. Roh, J.; Lyoo, J.; Hong, S. Enhanced Li-ion conductivity and air stability of sb-substituted Li_4GeS_4 toward all-solid-state Li-ion batteries. *ACS. Appl. Energy. Mater.* **2023**, *6*, 5446-55. DOI
118. Kaup, K.; Zhou, L.; Huq, A.; Nazar, L. F. Impact of the Li substructure on the diffusion pathways in alpha and beta Li_3PS_4: an *in situ* high temperature neutron diffraction study. *J. Mater. Chem. A.* **2020**, *8*, 12446-56. DOI
119. Kanazawa, K.; Yubuchi, S.; Hotehama, C.; et al. Mechanochemical synthesis and characterization of metastable hexagonal Li_4SnS_4 solid electrolyte. *Inorg. Chem.* **2018**, *57*, 9925-30. DOI
120. Tachez, M.; Malugani, J.; Mercier, R.; Robert, G. Ionic conductivity of and phase transition in lithium thiophosphate Li_3PS_4. *Solid. State. Ionics.* **1984**, *14*, 181-5. DOI
121. Kim, J. S.; Jung, W. D.; Choi, S.; et al. Thermally induced s-sublattice transition of Li_3PS_4 for fast lithium-ion conduction. *J. Phys. Chem. Lett.* **2018**, *9*, 5592-7. DOI
122. Jun, K.; Lee, B.; L, K. R.; Ceder, G. The nonexistence of a paddlewheel effect in superionic conductors. *Proc. Natl. Acad. Sci. U. S. A.* **2024**, *121*, e2316493121. DOI PubMed PMC
123. Smith, J. G.; Siegel, D. J. Low-temperature paddlewheel effect in glassy solid electrolytes. *Nat. Commun.* **2020**, *11*, 1483. DOI PubMed PMC
124. Zhang, Z.; Li, H.; Kaup, K.; Zhou, L.; Roy, P.; Nazar, L. F. Targeting superionic conductivity by turning on anion rotation at room temperature in fast ion conductors. *Matter* **2020**, *2*, 1667-84. DOI
125. Kuhn, A.; Holzmann, T.; Nuss, J.; Lotsch, B. V. A facile wet chemistry approach towards unilamellar tin sulfide nanosheets from $Li_{4x}Sn_{1-x}S_2$ solid solutions. *J. Mater. Chem. A.* **2014**, *2*, 6100-6. DOI
126. Winkler, C. Germanium, Ge, ein neues, nichtmetallisches element. *Ber. Dtsch. Chem. Ges.* **1886**, *19*, 210-1. DOI
127. Geller, S. The crystal structure of y Ag_8GeTe_6, a potential mixed electronic-ionic conductor. *Z. Kristallogr. Cryst. Mater.* **1979**, *149*, 31-48. DOI
128. Belin, R.; Aldon, L.; Zerouale, A.; Belin, C.; Ribes, M. Crystal structure of the non-stoichiometric argyrodite compound $Ag_{7-x}GeSe_5I_{1-}x$ (x=0.31). A highly disordered silver superionic conducting material. *Solid. State. Sci.* **2001**, *3*, 251-65. DOI
129. Kuhs, W. F.; Nitsche, R.; Scheunemann, K. The crystal structure of Cu_6PS_5Br, a new superionic conductor. *Acta. Crystallogr. B. Struct. Sci.* **1978**, *34*, 64-70. DOI
130. Kuhs, W.; Nitsche, R.; Scheunemann, K. The argyrodites - a new family of tetrahedrally close-packed structures. *Mater. Res. Bull.* **1979**, *14*, 241-8. DOI
131. Kong, S. T.; Deiseroth, H. J.; Reiner, C.; et al. Lithium argyrodites with phosphorus and arsenic: order and disorder of lithium atoms, crystal chemistry, and phase transitions. *Chemistry* **2010**, *16*, 2198-206. DOI
132. Deiseroth, H.; Maier, J.; Weichert, K.; Nickel, V.; Kong, S.; Reiner, C. Li_7PS_6 and Li_6PS_5X (X: Cl, Br, I): possible three-dimensional diffusion pathways for lithium ions and temperature dependence of the ionic conductivity by impedance measurements. *Z. Anorg. Allge. Chem.* **2011**, *637*, 1287-94. DOI
133. Gautam, A.; Sadowski, M.; Ghidiu, M.; et al. Engineering the site-disorder and lithium distribution in the lithium superionic argyrodite Li_6PS_5Br. *Adv. Energy. Mater.* **2021**, *11*, 2003369. DOI
134. Shannon, R. D. Revised effective ionic radii and systematic studies of interatomic distances in halides and chalcogenides. *Acta. Cryst. A.* **1976**, *32*, 751-67. DOI
135. Zhou, L.; Zhang, Q.; Nazar, L. F. Li-rich and halide-deficient argyrodite fast Ion conductors. *Chem. Mater.* **2022**, *34*, 9634-43. DOI
136. Schlem, R.; Ghidiu, M.; Culver, S. P.; Hansen, A.; Zeier, W. G. Correction to changing the static and dynamic lattice effects for the improvement of the ionic transport properties within the argyrodite Li_6PS_5.*x*SexI. *ACS. Appl. Energy. Mater.* **2020**, *3*, 4089-90. DOI
137. Morgan, B. J. Mechanistic origin of superionic lithium diffusion in anion-disordered Li_6PS_5 X argyrodites. *Chem. Mater.* **2021**, *33*, 2004-18. DOI PubMed PMC
138. Hanghofer, I.; Brinek, M.; Eisbacher, S. L.; et al. Substitutional disorder: structure and ion dynamics of the argyrodites Li_6PS_5Cl, Li_6

PS_5Br and Li_6PS_5I. *Phys. Chem. Chem. Phys.* **2019**, *21*, 8489-507. DOI

139. Ohno, S.; Helm, B.; Fuchs, T.; et al. Further evidence for energy landscape flattening in the superionic argyrodites $Li_{6+x}P_{1-x}M_xS_5I$ (M = Si, Ge, Sn). *Chem. Mater.* **2019**, *31*, 4936-44. DOI
140. Rayavarapu, P. R.; Sharma, N.; Peterson, V. K.; Adams, S. Variation in structure and Li^+-ion migration in argyrodite-type Li_6PS_5X (X = Cl, Br, I) solid electrolytes. *J. Solid. State. Electrochem.* **2012**, *16*, 1807-13. DOI
141. Kraft, M. A.; Ohno, S.; Zinkevich, T.; et al. Inducing high ionic conductivity in the lithium superionic argyrodites $Li_{6+x}P_{1-x}Ge_xS_5I$ for all-solid-state batteries. *J. Am. Chem. Soc.* **2018**, *140*, 16330-9. DOI
142. Rice, M.; Roth, W. Ionic transport in super ionic conductors: a theoretical model. *J. Solid. State. Chem.* **1972**, *4*, 294-310. DOI
143. Kanno, R.; Murayama, M. Lithium ionic conductor thio-LISICON: the Li_2S-GeS_2-P_2S_5 system. *J. Electrochem. Soc.* **2001**, *148*, A742. DOI
144. Kuhn, A.; Köhler, J.; Lotsch, B. V. Single-crystal X-ray structure analysis of the superionic conductor $Li_{10}GeP_2S_{12}$. *Phys. Chem. Chem. Phys.* **2013**, *15*, 11620-2. DOI PubMed
145. Kato, Y.; Hori, S.; Kanno, R. $Li_{10}GeP_2S_{12}$-type superionic conductors: synthesis, structure, and ionic transportation. *Adv. Energy. Mater.* **2020**, *10*, 2002153. DOI
146. Culver, S. P.; Squires, A. G.; Minafra, N.; et al. Evidence for a solid-electrolyte inductive effect in the superionic conductor $Li_{10}Ge_{1-x}Sn_xP_2S_{12}$. *J. Am. Chem. Soc.* **2020**, *142*, 21210-9. DOI